Soft Matter

REVIEW

View Article Online
View Journal

Cite this: DOI: 10.1039/d6sm00283h

The division of vesicles requires the fission of closed membrane necks but does not require active processes

Reinhard Lipowsky

One important objective of soft matter science and synthetic biology is to construct synthetic systems and processes that mimic the division of cells and organelles. Such division processes have been achieved experimentally for giant vesicles and *in silico* for nanovesicles. Here, we analyze recent studies of these division processes, focussing on results that have been obtained by our group, using a combination of theory, experiment, and simulation. We show that the division of vesicles requires the formation and fission of closed membrane necks but does not require chemomechanical coupling to active processes such as nucleotide hydrolysis. Closed membrane necks are formed when the vesicle volume is decreased or the membrane area is increased, provided the vesicle is enclosed by an asymmetric bilayer with a sufficiently large transbilayer asymmetry between its two leaflets. The membrane necks experience a constriction force that is controlled by the spontaneous curvature for giant vesicles and by the stress asymmetry for nanovesicles. A sufficiently large constriction force leads to neck fission and vesicle division as observed for vesicle membranes (i) with uniform lipid–protein composition, (ii) with intramembrane domains of distinct lipid–protein compositions, and (iii) in contact with condensate droplets. Most of these biomimetic division processes involve membrane proteins that act to increase the transbilayer asymmetry but none of them is coupled to an active process such as nucleotide hydrolysis.

Received 31st March 2026,
Accepted 20th May 2026

DOI: 10.1039/d6sm00283h

rsc.li/soft-matter-journal

1 Introduction

The vesicle membranes considered here share several fundamental properties with all cellular membranes. First, they consist of molecular bilayers formed by lipid molecules and membrane proteins as their basic and universal building blocks. Second, both vesicle bilayers and cellular membranes represent two-dimensional fluids. Third, this fluidity allows both types of membranes to remodel their shape, molecular composition, and topology. Here, we will emphasize the intimate relationship between shape and topological transformations as provided by the fission of closed membrane necks, which leads to the division of vesicles.

Membrane necks are intimately related to the budding of vesicles, during which a small membrane bud is expelled from the original mother vesicle. Giant unilamellar vesicles (GUVs) can form both out-buds, corresponding to spherical or prolate membrane segments that protrude into the exterior solution, as well as in-buds that are expelled towards the interior solution. One example for the formation of an in-bud is displayed in Fig. 1. The upper row of this figure displays giant vesicle shapes as observed experimentally in the Sackmann lab whereas the lower row depicts axisymmetric vesicle shapes as determined theoretically.[1] The formation of such in-buds from GUVs has been subsequently observed in many experimental studies.[2–11]

The in-budding of vesicles implies that the vesicle membranes consist of asymmetric lipid bilayers that prefer to bend

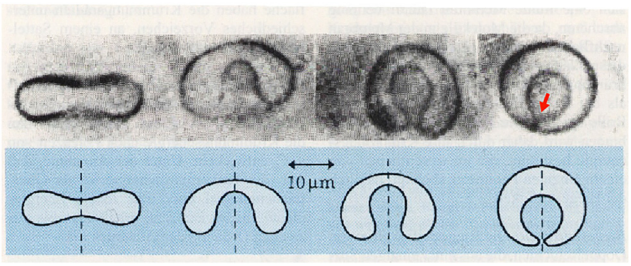

Fig. 1 In-budding of a giant unilamellar vesicle (GUV): the shape transformation starts from a discocyte shape, which resembles the shape of a red blood cell and transforms into a two-sphere shape. The two spherical segments are connected by a closed membrane neck (red arrow). The broken vertical lines are axes of rotational symmetry. Reused with permission from ref. 1 [Copyright 1990, EDPSciences].

Max Planck Institute of Colloids and Interfaces, Science Park Golm, 14424 Potsdam, Germany. E-mail: lipowsky@mpikg.mpg.de

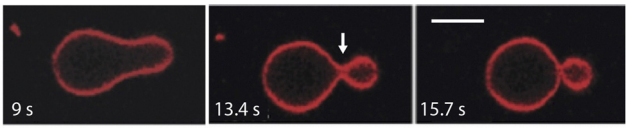

Fig. 2 Out-budding of a giant vesicle (red): the vesicle has a pear-like shape at time t = 9 s, which transforms into an out-budded two-sphere shape at t = 13.4 s. The two spherical segments are connected by a closed membrane neck (white arrow). This shape transformation is obtained for a sufficiently large and positive spontaneous curvature. Scale bar: 5 μm.[6]

towards the inner leaflet of the bilayer membrane. Within the theory of curvature elasticity, in-budding implies that the transbilayer asymmetry of the vesicle membrane can be characterized by a negative spontaneous curvature. On the other hand, a positive spontaneous curvature leads to out-budding of GUVs, for which one example is shown in Fig. 2. Out-budded GUVs have also been observed in many experimental studies.[12–27] For nanovesicles as shown in Fig. 3, budding processes are controlled by the stress asymmetry between the two bilayer leaflets.[28,29]

The closed membrane necks of out- and in-buds experience constriction forces[19,30] that compress the necks until they undergo fission and induce the division of the out- or in-budded vesicles. Such fission processes have been observed for a variety of synthetic vesicle systems, which include: GUV membranes with a uniform lipid composition and doped with His-tagged green fluorescent proteins (GFPs);[19] GUV membranes with intramembrane domains that have distinct lipid–protein compositions;[27] formation and fission of membrane necks by three proteins of the endosomal sorting complex required for transport (ESCRT) without the ATPase Vps4;[4,5,9] and nanovesicle membranes in contact with condensate droplets.[31] In general, the process of neck closure can follow different pathways and may proceed in an axi-symmetric or non-axisymmetric manner. In particular, several such pathways must be distinguished for the closure of membrane necks during the complete engulfment of condensate droplets.[32] Most of the biomimetic division processes mentioned above involve membrane proteins that act to increase the transbilayer asymmetry but none of them is coupled to an active process such as nucleotide hydrolysis.

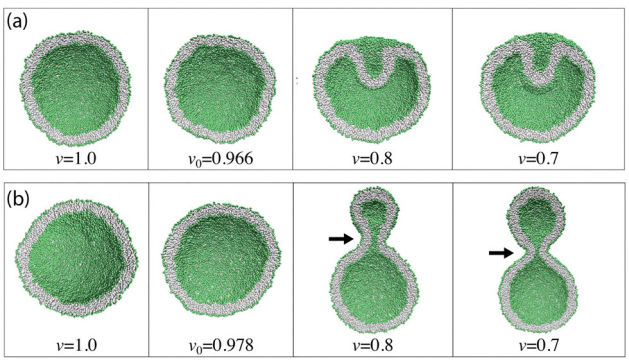

Fig. 3 Budding of nanovesicles as observed in molecular dynamics simulations.[28] The budding process is induced by decreasing the volume parameter ν of nanovesicles from ν = 1 to ν = 0.7. The direction of budding is controlled by the two leaflet tensions of the spherical bilayer: (a) formation of an in-bud for a spherical vesicle with a and a stretched outer and a compressed inner leaflet; and (b) formation of an out-bud for a spherical vesicle with a compressed outer and a stretched inner leaflet.[28] The closed membrane necks in (b) are indicated by black arrows. Note that these nanoscale necks have an hour-glass shape.

In the context of bioenergetics, an active process is an exergonic chemical reaction that reduces the free energy of the biosystem and, thus, moves the system 'downhill' in its free energy landscape.[33] Exergonic processes can occur spontaneously without any free energy input into the biosystem but are often catalyzed by proteins that act as enzymes for the chemical reaction, thereby reducing the free energy barrier encountered by this reaction. Endergonic processes, on the other hand, increase the free energy of the biosystem, which then has to move 'uphill' in its free energy landscape. Therefore, endergonic processes do not occur spontaneously, apart from rare fluctuations that subsequently decay back into a state of lower free energy. However, endergonic processes can be coupled to exergonic processes in such a way that the combination of both processes leads to an overall reduction of the system's free energy.

In the literature, it is often emphasized that active processes move the biosystems ''out of equilibrium''. However, it seems more appropriate to emphasize the free energy transduction[34] arising from the coupling between active or exergonic 'downhill' processes and endergonic 'uphill' processes.

Protein-catalyzed hydrolysis of nucleotides such as ATP or GTP are particularly important examples for exergonic chemical reactions because they can drive many endergonic processes, both *in vivo* and *in vitro*. In particular, nucleotide hydrolysis can drive endergonic mechanical processes such as motor transport or membrane deformations, thereby providing examples for the chemomechanical coupling between exergonic chemical reactions and endergonic mechanical processes.†

In this paper, we will focus on vesicle division processes without chemomechanical coupling, that is, without the coupling to active processes that drive this division. Indeed, as explained in Section 4, the division of GUVs with uniform lipid–protein bilayers can be induced and controlled by curvature-elasticity alone without any coupling to exergonic chemical reactions. Likewise, Sections 6, 7, and 9 demonstrate that curvature-induced neck fission and vesicle division without the involvement of active processes is observed for (i) vesicle membranes with intramembrane domains,[27] (ii) membrane necks generated by three proteins of the endosomal sorting complex required for transport (ESCRT),[4,5,9] and (iii) nanovesicles interacting with condensate droplets.[31] Section 5 describes active shape oscillations of GUVs driven by Min proteins and ATP hydrolysis.[18,20] In fact, these active shape oscillations involve the cyclic closure and opening of membane necks. However, in contrast to what one might expect, the

† Some authors prefer to use the term mechano-chemical coupling.

membrane necks do not undergo fission and the GUVs do not divide.

The literature on the division of cells and organelles often emphasizes the coupling of these division processes to nucleotide hydrolysis as catalyzed by membrane proteins. These proteins include dynamin,[35–37] ESCRT-III proteins[4,5,9] together with the ATPase Vps4,[4,38,39] and the bacterial protein FtsZ.[40–43] Dynamin generates constriction forces at membrane necks coupled to GTP hydrolysis. Three ESCRT-III proteins are sufficient to form and cleave membrane necks,[4,5,9] see Section 7 below, while the ATPase Vps4 is only required for the disassembly of the ESCRT-III complex from the membrane after neck fission has been completed.[4] The bacterial protein FtsZ polymerizes into a ring under the membrane, and this ring contracts to initiate division of the bacterial cell,[40,42] a process that is coupled to GTP hydrolysis.[40,41,43] The chemomechanical coupling between nucleotide hydrolysis and the membrane proteins dynamin, ESCRT-III together with Vps4, and FtsZ is important in order to understand the fission process *in vivo* but is difficult to reconstitute *in vitro*. The reconstitution of FtsZ in GUVs, for instance, has been pursued for more than a decade[44–46] but FtsZ-induced division of vesicles has not been achieved so far. Therefore, curvature-induced fission of membrane necks without any chemomechanical coupling as described here provides a simple and useful approach for the division of vesicles in the context of soft matter science and synthetic biology.

The paper is organized as follows. First, in the next Section 2, we discuss the formation of membrane necks during vesicle budding in more detail. In addition, we show that vesicles can form multispherical shapes with several necks and that all necks can be characterized by relatively simple geometric properties. We also emphasize in Section 2 that closed membrane necks provide a direct connection between the remodeling of vesicle shape and the remodeling of vesicle topology. The subsequent Section 3 addresses the elasticity of fluid membranes, which undergo two types of elastic deformations, membrane stretching and compression as well as membrane bending and flattening. Membrane stretching and compression are controlled by mechanical membrane tension whereas membrane bending and flattening are controlled by curvature elasticity. Division of GUVs *via* His-tagged GFP is addressed in Section 4; the absence of division for GUVs that undergo active shape oscillations in Section 5; division of GUVs with intramembrane domains in Section 6; division of GUVs *via* three ESCRT protein but without nucleotide hydrolysis in Section 7; different pathways for neck formation of GUVs interacting with condensate droplets in Section 8; and neck formation and division of nanovesicles induced by condensate droplets in Section 9. At the end, we provide a summary and a brief outlook on related membrane processes.

2 Vesicle shapes with membrane necks

In this section, we provide more examples for the formation of membrane necks as observed for giant vesicles by optical microscopy and for nanovesicles by molecular dynamics simulations.

2.1 Closed membrane necks of giant vesicles

The formation of membrane necks during in-budding and out-budding of giant vesicles is depicted in Fig. 1 and 2. In both cases, the closed membrane neck provides a connection between a large sphere of radius R_l and a small sphere of radius R_s. Both spheres are punctured at the neck in the sense that the membrane curvature exhibits a jump as we move across the neck from the large to the small sphere or *vice versa*. For the out-budded shape in Fig. 2, both spheres have a positive mean curvature as given by $M_l = +1/R_l$ and $M_s = +1/R_s$. For the in-budded shape in Fig. 1, the large sphere has again a positive mean curvature, $M_l = +1/R_l$, but the small sphere now has a negative mean curvature, $M_s = -1/R_s$.

For the vesicles in Fig. 1 and 2, the two radii R_l and R_s as well as the two mean curvatures M_l and M_s can be directly read off from the optical images and can be used to define the effective mean curvature M_{ls}^{eff} of closed (ls)-necks *via*[30]

$$M_{ls}^{eff} \equiv \frac{1}{2}(M_l + M_s) = \frac{1}{2}\left(\frac{1}{R_l} \pm \frac{1}{R_s}\right) \quad (1)$$

which interpolates between the two mean curvatures M_l and M_s of the large and small sphere in a symmetric manner. The effective mean curvature is positive for the closed neck of an out-bud but negative for the closed neck of an in-bud. It is now convenient to use the sign of the neck's effective mean curvature to distinguish positive from negative membrane necks. Thus, positive and negative membrane necks are characterized by positive and negative values of the effective mean curvature M_{ls}^{eff} of these necks. This distinction continues to apply for multispheres consisting of more than two spheres connected by more than one neck as in Fig. 4.

The second equality in eqn (1) is based on the simple geometric relations between the mean curvatures and the radii of spheres. However, the first equality in eqn (1) remains valid even if the membrane segments adjacent to the closed

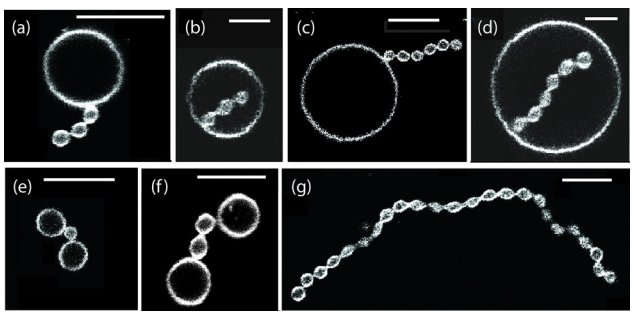

Fig. 4 Multispherical shapes of giant vesicles consisting of large spheres with radius R_l and small spheres with radius R_s.[6] Using the definition for the effective mean curvature M_{ls}^{eff} of a neck, each neck in panels (a)–(c) has an effective mean curvature M_{ls}^{eff} that is positive whereas each neck in panels (d)–(f) has such a curvature that is negative as follows from the definition of M_{ls}^{eff} in eqn (1). The multisphere in panel (g) consists of 24 equally sized spheres with radius R_* connected by 23 positive necks.

membrane neck do not attain spherical shapes. The mean curvatures M_l and M_s are then equal to the local mean curvatures adjacent to the neck. One example is provided by small spheres that transforms into small prolates for sufficiently large and positive values of the spontaneous curvature[30] as observed experimentally for out-budded GUVs.[19]

2.1.1 Stability of positive necks against neck opening. A positive (ls)-neck connecting a large and a small sphere is stable if the positive effective mean curvature M_{ls}^{eff} of this neck does not exceed the positive spontaneous curvature m of the membrane.[30] Thus, a positive (ls)-neck is stably closed if it satisfies the stability condition[47,48]

$$0 < M_{ls}^{eff} \leq m \quad \text{(stable positive neck)}. \tag{2}$$

The limiting cases with $M_{ls}^{eff} = m$ correspond to limit shapes that separate shapes with closed from shapes with open (ls)-necks in the morphology diagram, see the example for positive two-sphere shapes in Fig. 8, which involves two lines of limit shapes denoted by L_{1+1}^{pos} and L_{2*}^{pos}.

2.1.2 Stability of negative necks against neck opening. On the other hand, a negative (ls)-neck connecting two membrane segments k and l is stable if if the negative effective mean curvature M_{ls}^{eff} of this neck does not exceed the negative spontaneous curvature m of the membrane.[30] Thus, a negative (ls)-neck is stably closed if it satisfies the stability condition[47,49]

$$M_{ls}^{eff} \leq m < 0 \quad \text{(stable negative neck)}. \tag{3}$$

The limiting cases with $M_{ls}^{eff} = m$ again correspond to limit shapes that separate closed from open (ls)-necks in the corresponding morphology diagram.

2.2 Multispherical shapes of giant vesicles

Some examples for multispherical shapes are shown in Fig. 4. All multispheres involve at most two different sphere radii a large one with radius R_l and a small one with radius R_s. This property is a direct consequence of the shape equation for spherical membrane segments.[6,50] Furthermore, for an out-budded multisphere as in Fig. 4a, c, e and f all necks are positive, that is, all pairs of punctured spheres i and j that are connected by closed membrane necks exhibit positive values of the effective mean curvature

$$M_{ij}^{eff} \equiv \frac{1}{2}(M_i + M_j). \tag{4}$$

In contrast, all necks of an in-budded vesicle as in Fig. 4b and d are negative and characterized by $M_{ij}^{eff} < 0$.

2.2.1 Different types of membrane necks. Inspection of Fig. 4 shows that multispherical shapes typically involve different types of membrane necks.[50] For multispheres with $R_l > R_s$, we can distinguish (ls)-necks between one large and one small sphere from (ss)-necks between two small spheres and (ll)-necks between two large spheres. In addition, it is also useful to distinguish the (**)-necks of multispheres with $R_l = R_s = R_*$ as in Fig. 4g from those with $R_l > R_s$. However, for all of these necks, we can apply the definition of the effective mean curvature M_{ij}^{eff} in eqn (4) using an appropriate identification of the two subscripts i and j with one of the subscripts l, s, or *. The stability conditions for any type of neck against neck opening is then given by $0 < M_{ij}^{eff} \leq m$ for positive (ij)-necks and by $M_{ij} \leq m < 0$ for negative (ij)-necks.

2.2.2 Positive and negative multispheres. The property that all membrane necks of a given multisphere have the same sign allows us to further simplify the terminology and to distinguish positive from negative multispheres. Positive multispheres as in Fig. 4a, c, e and f are formed for positive spontaneous curvature and involve only positive necks. On the other hand, negative multispheres as in Fig. 4b and d are formed for negative spontaneous curvature and involve only negative necks.

2.2.3 Multispheres with N_l large and N_s small spheres. Each multisphere in Fig. 4 is built up from N_l large and N_s small spheres, thereby forming an $(N_l + N_s)$-sphere. Both the positive (1 + 6)-sphere in Fig. 4c and the negative (1 + 6)-sphere in Fig. 4d consist of one large and six small spheres whereas the (2 + 2)-sphere in Fig. 4f is built up from two large and two small spheres. In general, each $(N_l + N_s)$-sphere is stable within a certain stability regime, corresponding to a subregion of the morphology diagram for the vesicle shapes.[50,51] One example is provided by the stability regime for positive (1 + 1)-spheres as displayed in Fig. 8 below.

2.2.4 Multispheres as constant-mean-curvature surfaces. The vesicle shape in Fig. 4g provides an example for a multispherical shape consisting of equally sized spheres, for which $R_l = R_s \equiv R_*$. In this case, the vesicle membrane forms a constant-mean-curvature surface with mean curvature $M_* = 1/R_*$ apart from the necks. Furthermore, all necks have the same effective mean curvature $M_{**}^{eff} = 1/R_*$. Therefore, the vesicle shape in Fig. 4g represents a constant-mean-curvature surface with constant mean curvature $M_* = M_{**}^{eff} = 1/R_*$. In fact, all other multispherical shapes in Fig. 4 can be regarded as generalized constant-mean-curvature surfaces with two piece-wise constant mean curvatures.[50]

2.3 Budding of nanovesicles

The budding of nanovesicles has been studied by molecular dynamics simulations. Two examples for such budding processes are displayed in Fig. 3a and b. In both examples, the initial condition for the simulations is provided by spherical vesicles with an outer radius of about 40 nm, corresponding to the first snapshots in Fig. 3a and b. The spherical vesicles in these two panels have the same volume and are assembled from the same total number of lipids in the two leaflets of the vesicle bilayers but differ in the number of lipid molecules that are assembled in each leaflet. Let us denote the number of lipids assembled in the outer and inner leaflet by N_{ol} and N_{il}, respectively. These lipid numbers do not change on the time scales of the simulations and thus represent useful control parameters for these simulations.

The nanovesicles in Fig. 3a and b are assembled from the same total number of lipids, $N_{ol} + N_{il} = 10\,100$, but differ in the lipid numbers assembled within the two bilayer leaflets. Thus,

the outer and inner leaflets of the nanovesicle in Fig. 3a consist of $N_{ol} = 5700$ and $N_{il} = 4400$ lipids whereas the nanovesicle in Fig. 3b contains $N_{ol} = 6300$ and $N_{il} = 3800$ lipids.[28] Even though the iipid numbers N_{ol} and N_{il} represent useful control parameters for the *in silico* assembly, they provide only limited insight into the mechanical and elastic states of the lipid bilayers and their leaflets. Indeed, each leaflet of the bilayer membrane can be stretched or compressed when it is subject to a positive or negative leaflet tension.

2.3.1 Leaflet tensions. The leaflet tensions Σ_{ol} and Σ_{il} in the outer and inner leaflets of the nanovesicles can be computed from the stress profiles across the vesicle bilayers. For each ensemble of bilayers with the same total number of lipids, $N_{ol} + N_{il}$, one then finds a unique reference state with tensionless leaflets, that is, with $\Sigma_{ol} = \Sigma_{il} = 0$. For total lipid number $N_{ol} + N_{il} = 10\,100$ as in Fig. 3, the reference state with tensionless leaflets is obtained for $N_{ol} = N_{ol}^* = 5993$ and $N_{il} = N_{il}^* = 10\,100 - N_{ol}^* = 4107$.[28,29]

The sum $\Sigma_{il} + \Sigma_{ol}$ of the two leaflet tensions is equal to the bilayer tension Σ. The reference state of the bilayer is then characterized by $\Sigma = \Sigma_{ol} + \Sigma_{il} = 0$. To avoid membrane rupture, the vesicle membranes are taken to experience only a low bilayer tension. However, even for vanishing bilayer tension, $\Sigma = \Sigma_{il} + \Sigma_{ol} = 0$, the individual leaflets can still experience significant leaflet tensions if one leaflet is stretched by a positive leaflet tension whereas the other leaflet is compressed by a negative and opposite leaflet tension, that is, if the two leaflet tensions satisfy $\Sigma_{ol} = -\Sigma_{il}$.

For the two nanovesicles in Fig. 3a and b, the bilayer tension Σ vanishes for volume parameter $\nu = \nu_0$, for which the vesicle shape is displayed in the second column of Fig. 3. In panel (a) of this figure, the outer leaflet tension is $\Sigma_{ol} = +0.87$, corresponding to a stretched outer leaflet, whereas the inner leaflet tension is $\Sigma_{il} = -0.82$, corresponding to a compressed inner leaflet. In the second panel of Fig. 3b, the outer and inner leaflet tensions are $\Sigma_{ol} = -0.99$ and $\Sigma_{il} = +0.99$, corresponding to a compressed outer and a stretched inner leaflet. All tension values are in units of k_BT/d^2 where d is the bead diameter of the coarse-grained molecular model.[28]

2.3.2 Leaflet tension space and stress asymmetry of nanovesicles. The two leaflet tensions Σ_{il} and Σ_{ol} span a two-dimensional parameter space for nanovesicles, which defines the leaflet tension space.[29,52] The origin $(\Sigma_{il},\Sigma_{ol}) = (0,0)$ of this space corresponds to the relaxed reference state with tensionless leaflets. The four quadrants of the $(\Sigma_{il},\Sigma_{ol})$-plane represent bilayers with four possible combinations of stretched and compressed leaflets. To characterize the elastic response of the two leaflets, it is also instructive to change variables from the leaflet tensions Σ_{il} and Σ_{ol} to the bilayer tension $\Sigma = \Sigma_{ol} + \Sigma_{il}$ and the stress asymmetry defined by[29,53]

$$\Delta\Sigma_{ve} \equiv \Sigma_{ol} - \Sigma_{il}. \tag{5}$$

States of the vesicle bilayer with vanishing stress asymmetry, $\Delta\Sigma_{ve} = 0$, are located on the main diagonal of the $(\Sigma_{il},\Sigma_{ol})$-plane whereas states with vanishing bilayer tension, $\Sigma = 0$, are found along the secondary diagonal, which is perpendicular to the main diagonal. In general, all bilayer states above the secondary diagonal in the $(\Sigma_{il},\Sigma_{ol})$-plane are stretched by a positive bilayer tension $\Sigma > 0$, whereas those below the secondary diagonal are compressed by a negative bilayer tension $\Sigma < 0$. Likewise, all bilayer states above and below the main diagonal exhibit a positive and negative stress asymmetry, $\Delta\Sigma > 0$ and $\Delta\Sigma < 0$, respectively.

2.4 Closed membrane necks at different length scales

A comparison of Fig. 3b with Fig. 2 reveals that closed membrane necks look quite different when we view them with nanoscale or micron scale resolution. In the last two panels of Fig. 3b, the black arrows point to closed membrane necks as observed in molecular dynamics simulations. The lipid bilayer has a thickness of about 4 nm and forms necks with an hourglass-like shape. The neck is axisymmetric and has a circular waistline. For a closed neck, the outer radius of this waistline is equal to the bilayer thickness whereas the inner radius vanishes. Inspection of the simulation snapshots in Fig. 3b shows that the hourglass-shaped neck is highly curved in the sense that its contour curvature is large and negative.

At the micron scale, the optical microscopy view of the closed membrane neck is quite different, see white arrow in Fig. 2. Indeed, when viewed with optical microsopy, the hourglass-shaped membrane segment is no longer visible but is replaced by the touching point of the two spheres connected by the neck. Thus, one might view the point-like neck as a direct consequence of the limited optical resolution. It turns out, however, that this point-like neck correctly captures two important properties of the neck. First, during neck closure, the two principal curvatures diverge but the mean curvature attains a finite limit. Second, this mean curvature of the neck is directly related to the curvature radii of the two adjacent membrane segments, which can be directly read off from the optical images.

2.4.1 Closure of hourglass-shaped neck. We will now discuss the closure of the hour-glass shape in more detail. In Fig. 3b, the waistline (wl) of the hourglass-shaped neck forms a circle with radius R_{ne}. Along this waistline, the neck is characterized by two principal curvatures, the negative contour curvature $C_{1,wl} < 0$ perpendicular to the waistline and the positive principal curvature $C_{2,wl} = 1/R_{ne} > 0$ parallel to the waistline. When the neck closes, the neck radius goes to zero and the principal curvature $C_{2,wl}$ diverges. However, the mean curvature

$$M_{wl} = \frac{1}{2}\left(C_{1,wl} + C_{2,wl}\right) \tag{6}$$

remains finite and satisfies the asymptotic equality

$$M_{wl} \approx M_{ls}^{eff} = \frac{1}{2}(M_l + M_s) \tag{7}$$

in the limit of small R_{ne} with the effective mean curvature M_{ls}^{eff} as given by eqn (1).[20,50] Thus, as the neck closes, the positive singular contribution from the second principal

curvature $C_{2,\mathrm{wl}} = 1/R_{\mathrm{ne}} > 0$ is cancelled by the negative singular contribution arising from the contour curvature $C_{1,\mathrm{wl}}$, which corresponds to the shape of a singular catenoid. The remaining effective neck mean curvature $M_{\mathrm{ls}}^{\mathrm{eff}}$ has a finite value, which can be positive or negative depending on the mean curvatures of the large and small spheres connected by the neck.

2.5 Topological changes *via* fission of membrane necks

So far, we looked at stable membrane necks of GUVs and nanovesicles as observed experimentally and in simulations. The stable necks of GUVs satisfy the stability conditions in eqn (2) and (3) with M_{ls} replaced by M_{ij}. These stability conditions determine the stability regimes against neck opening. One example is provided by the stability regime of positive two-spheres as determined theoretically and experimentally in Fig. 8 and 9 below. However, the most significant instability of a closed neck is provided by the fission of this neck, which leads to the division of a single vesicle into two daughter vesicles. Such a division process represents a topological transformation from a one-vesicle to a two-vesicle state. As a consequence, membrane necks provide a direct connection between the remodeling of vesicle shape and the remodeling of vesicle topology.

The division of vesicles *via* the fission of membrane necks is schematically displayed in Fig. 5 for out-budded and in-budded two-sphere vesicles. The division of an out-budded vesicle as in Fig. 5a leads to two separate daughter vesicles as in Fig. 5b. The two daughter vesicles can then freely diffuse away from each other within the exterior solution. In contrast, the division of an in-budded vesicle as in Fig. 5c leads to two nested daughter vesicles with the smaller daughter vesicle inside the larger one. In this case, the smaller daughter vesicle can not escape from the larger one.

In later sections, we will describe several biomimetic division processes including (i) the division of GUVs with uniform lipid–protein bilayers; (ii) the division of vesicles with intramembrane domains arising from lipid phase separation within the membranes, and (iii) the division of nanovesicles in contact with condensate droplets. In order to discuss these division processes in a systematic manner, we first need to briefly review the elastic properties of fluid membranes.

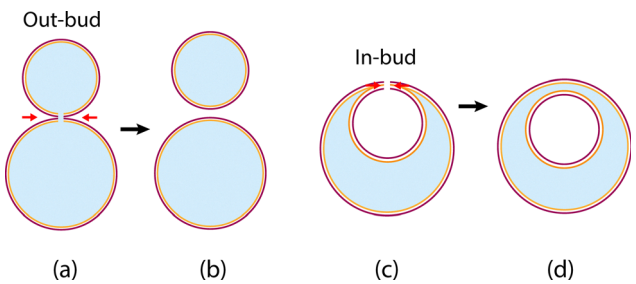

Fig. 5 Division of two-sphere vesicles into two daughter vesicles by fission of membrane necks (red arrows): (a) and (b) division of out-budded vesicle by the fission of a positive membrane neck; and (c) and (d) division of an in-budded vesicle by fission of a negative membrane neck. The division process of an out-budded vesicle leads to two separate daughter vesicles as in (b) whereas the division of an in-budded vesicle generates two nested daughter vesicles as in (d).

3 Elasticity of fluid membranes

We now view the biomembrane as a thin elastic sheet. According to classical elasticity theory,[54] such a sheet can exhibit three different elastic deformations as displayed in Fig. 6. The shearing deformation in Fig. 6c does not represent a reversible deformation, however, because such a deformation leads to hydrodynamic flow within the membrane. Therefore, a thin fluid-elastic sheet exhibits only two elastic deformations, stretching and bending. These deformations are reversible: the opposite of membrane stretching is membrane compression whereas the opposite of membrane bending is membrane flattening. In Fig. 6, reversible deformations are indicated by a double-arrow whereas the irreversible shearing deformations is labeled by a single arrow. The stretching and compression of membranes is governed by membrane tension whereas the bending and flattening of membranes is controlled by curvature elasticity. These control parameters will be briefly described in the next two subsections.

3.1 Curvature elasticity

3.1.1 Curvature and bending energies. The bending and flattening deformations of a fluid membrane are controlled by curvature elasticity. In the spontaneous curvature model,[30,47,55] curvature elasticity is described by the curvature energy

$$E_{\mathrm{cu}} = \int \mathrm{d}A \left[2\kappa(M-m)^2 + \kappa_{\mathrm{G}} G\right]. \tag{8}$$

where $\int \mathrm{d}A$ represents an integral over the membrane's surface area A. The curvature energy E_{cu} in eqn (8) depends on two geometric quantities, the (local) mean curvature M and the (local) Gaussian curvature G of the membrane, as well as on three curvature-elastic parameters, the bending rigidity κ, the

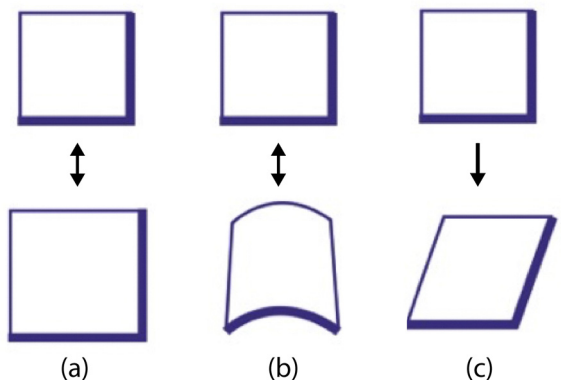

Fig. 6 When biomembranes are viewed as thin elastic sheets, three different elastic deformations can be distinguished: (a) stretching and compression; (b) bending and flattening; as well as (c) shearing. The double-arrows in (a) and (b) indicate reversible deformations of a fluid-elastic sheet whereas the single arrow in (c) indicates that shearing represents an irreversible deformation because it leads to hydrodynamic flow within the membrane.

spontaneous curvature m, and the Gaussian curvature modulus κ_G. For membranes with a laterally uniform composition, the three curvature-elastic parameters are laterally uniform as well. For such a laterally uniform vesicle membrane, the Gaussian curvature energy E_G as defined by the second term in eqn (8) becomes

$$E_G = \kappa_G \int dA G = 2\pi\chi\kappa_G = 2\pi(2-2g)\kappa_G \quad (9)$$

in the absence of membrane pores or edges, with the Euler characteristic χ and the topological genus as follows from the Gauss–Bonnet theorem.[56] If the vesicle undergoes a shape transformation that does not change its topology, the Gaussian curvature energy E_G in eqn (9) is a topological constant and the vesicle shapes depend only on the membrane's bending energy

$$E_{be} = \int dA 2\kappa(M-m)^2. \quad (10)$$

This energy fulfills the inequality $E_{be} \geq 0$, with $E_{be} = 0$ for constant mean curvature $M = m$. In practise, the vesicle membrane can only partially adapt its mean curvature to the spontaneous curvature unless the vesicle forms a sphere or multisphere with constant mean curvature $M = m$.

Even though the bending energy as given by eqn (10) is relatively simple, it has been recently shown to provide a quantitative description for the shapes of giant vesicles when the vesicle membranes contain at least one molecular component such as cholesterol that undergoes frequent flip-flops.[6,19]

3.1.2 Curvature-elastic tension.‡ To introduce the curvature-elastic tension, let us consider a flat membrane segment with vanishing mean curvature $M = 0$ but nonzero spontaneous curvature m. It then follows from the bending energy E_{be} in eqn (10) that such a flat membrane segment of area A has the bending energy $2\kappa m^2 A$. Therefore, flattening of a membrane segment, which has the spontaneous curvature m and would prefer to attain a curved conformation with mean curvature $M = m$, is governed by the curvature-elastic tension[30,57]

$$\sigma \equiv 2\kappa m^2 \quad (11)$$

which represents a material parameter that is proportional to the bending rigidity κ and increases quadratically with the spontaneous curvature m. Depending on the lipid composition and the transbilayer asymmetry, the curvature-elastic tension varies over seven orders of magnitude.[57] Furthermore, the curvature-elastic tension σ as defined by eqn (11) can be directly measured by micropipette aspiration of tubulated GUVs as well as by repeated cycles of osmotic deflation and inflation of such GUVs.[58]

3.2 Membrane tension of biomimetic membranes

From an intuitive point of view, membrane tension acts to stretch or compress the membrane as shown schematically in Fig. 6a, thereby changing the surface area of the membrane. However, this intuitive view represents an oversimplification because it ignores the difficulty to measure membrane tension and obscures important conceptual issues.

First, changes of the membrane's surface area are necessarily small because the membrane ruptures when its area is stretched beyond a few percent. As a consequence, changes in the membrane's surface area are very difficult to measure.

3.2.1 Composite nature of membrane tension. Second, it follows from the theory of curvature elasticity that the total membrane tension Σ_{tot} can be decomposed into two terms, the mechanical membrane tension Σ, which acts to stretch or compress the membrane as in Fig. 6a, and the curvature-elastic tension $\sigma = 2\kappa m^2$ as in eqn (11). For tubulated GUVs, the total membrane tension Σ_{tot} is dominated by the curvature-elastic tension σ because, for such GUVs, σ is much larger than the mechanical membrane tension Σ.[57] One should also note that, for about 40 years, the mechanical membrane tension Σ was distinguished from the Lagrange multiplier (or auxiliary) tension conjugate to membrane area that enters the shape functional for the constrained minimization of the bending energy[30,59] but these two tensions are, in fact, identical. This identity follows from the minimization of the combined bending and stretching energy for a compressible membrane, neglecting the small membrane area that may be stored in the membrane's shape fluctuations.[49]

3.2.2 Mechanical membrane tension is fundamentally different from interfacial tension. Third, the literature on membrane tension is very confusing and full of misconceptions. In particular, the mechanical tension of a membrane has often been treated as the interfacial tension of a liquid–liquid interface,[60–67] in close analogy to thin liquid films and soap bubbles.[68–70] It is important to note, however, that interfacial tension and mechanical membrane tension have fundamentally different properties.[71] Indeed, interfacial tensions are always positive whereas mechanical membrane tensions can be positive or negative and then lead to membrane stretching or compression as in Fig. 6a. As a consequence, lipid bilayers can attain five different elastic states depending on the stretching or compression of their two leaflets but only bilayer states with two stretched leaflets are analogous to soap films.[71] Furthermore, the mechanical membrane tension of a vesicle membrane depends on the vesicle's size and shape as one can explicitly demonstrate by computing the mechanical tension of multispherical vesicle shapes as in Fig. 4.[30,50]

3.2.3 Fluctuation tension for shape fluctuations. Fourth, at finite temperature T, membranes undergo thermally-excited shape fluctuations or bending undulations in order to increase their configurational entropy. These shape fluctuations correspond to normal displacements of the membrane from its average shape and lead to a characteristic flicker spectrum, which is rather different from the corresponding spectrum for the shape fluctuations of a liquid–liquid interface.[71]

In fact, in contrast to liquid–liquid interfaces, fluid membranes have a finite persistence length ξ_p for the correlations of their normal vectors, with different types of shape fluctuations on length scales below and above the persistence length.

‡ Here and below, the term "curvature-elastic tension" replaces the term "spontaneous tension" as originally used in ref. 57.

The persistence length of tensionless membranes depends exponentially on the ratio of the bending rigidity κ to the thermal energy k_BT[72–74] and is thus rather large for phospholipid bilayers with $\kappa \backsimeq 20k_BT$ at room temperature.

On length scales which are large compared to the persistence length, tensionless membranes attain crumpled states with no average orientation of their normal vectors as observed in Monte Carlo simulations of dynamically triangulated membrane surfaces.[74] On the other hand, in the presence of a positive mechanical membrane tension $\Sigma > 0$, membranes form bilayer pores on sufficiently large length scales.[75,76] Therefore, in the thermodynamic limit of a large membrane segment, the membrane becomes either crumpled for $\Sigma = 0$ or porated for $\Sigma > 0$. As a consequence, there is no meaningful thermodynamic limit of a fluid membrane and thus no thermodynamic definition of the mechanical membrane tension, again in contrast to the interfacial tension of a liquid–liquid interface, for which the thermodynmic definition was introduced a long time ago by J. Willard Gibbs.[77,78]

4 Controlled division of giant vesicles

4.1 Morphology diagram of lipid vesicles

For a lipid vesicle at constant temperature, the vesicle volume V is determined by the osmotic conditions in the interior and exterior aqueous solutions while the surface area A of the lipid bilayer is controlled by the number of lipids assembled in this bilayer. As a consequence, such a vesicle undergoes isothermal shape transformations at constant vesicle volume V and at constant membrane area A. For a vesicle membrane with laterally uniform composition, all shapes of the vesicle can be displayed in a two-dimensional morphology diagram that depends on two dimensionless shape parameters.[47]

The basic length scale for the vesicle shape is conveniently defined in terms of the vesicle's surface area A *via* $R_{ve} \equiv \sqrt{A/(4\pi)}$. The two dimensionless shape parameters that span the morphology diagram are then given by the volume-to-area ratio

$$\bar{v} \equiv \frac{V}{\frac{4\pi}{3}R_{ve}{}^3} = 6\sqrt{\pi}\frac{V}{A^{3/2}} \qquad (12)$$

and by the rescaled spontaneous curvature $\bar{m} = mR_{ve}$. In order to determine such a diagram experimentally, one needs to vary $\bar{v}$ and $\bar{m}$ independently. The volume-to-area ratio $\bar{v}$ can be varied by changes in the osmotic conditions. The quantitative control of the spontaneous curvature $\bar{m}$ is more difficult but has been recently achieved by low densities of His-tagged proteins that bind to the vesicle membrane and can be used ro fine-tune its spontaneous curvature.[19]

4.2 Fine-tuning of spontaneous curvature

The spontaneous curvature of a GUV membrane can be controlled by exposing the GUVs to an exterior solution of His-tagged proteins, which bind to the membrane *via* certain anchor lipids such as DGS-NTA(Ni) lipids.[19,79] In order to increase the configurational and translational entropies of the membrane-bound GFPs, the membrane bends away from these proteins as shown in Fig. 7. Therefore, the GFP molecules create a certain bilayer asymmetry or spontaneous curvature m of the GUV membrane. The magnitude of m increases with the coverage of the membrane by the GFPs as in eqn (13) below.

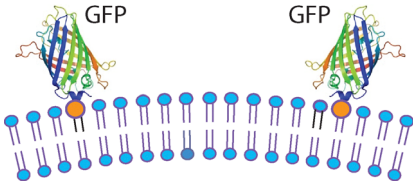

Fig. 7 Bilayer asymmetry and spontaneous curvature generated by green fluorescent protein (GFP) molecules at the outer leaflet of a GUV membrane. Each GFP has a His-tag, by which it binds to an anchor lipid (orange headgroup). The spontaneous curvature m increases with the coverage Γ of the membrane by the GFP molecules as in eqn (13). It follows from the experimental study in ref. 19 that the average spatial separation of the membrane-bound GFPs is at least 25 nm, which is significantly larger than the GFP's lateral size of about 3 nm.

The GFP coverage Γ of the membrane is defined by the number of membrane-bound proteins per unit membrane area. This coverage depends on the molar concentration X of the His-tagged proteins in the exterior solution and on the mole fraction of the anchor lipids in the membrane. To directly measure the coverage Γ, it is particularly useful to consider His-tagged proteins that are fluorescent as well. The coverage Γ can then be obtained by calibrating the fluorescence intensity of the membrane-bound proteins.

Using such a calibration method for green fluorescent proteins (GFPs), the coverage Γ of His-tagged GFP was observed to be proportional to the molar concentration X of the protein in the exterior solution over a wide concentration range. Furthermore, a quantitative analysis of the vesicle shapes showed that the spontaneous curvature m is proportional to the coverage Γ and given by[19]

$$m = \Gamma \times 27\ \text{nm} = \frac{\alpha}{\mu\text{m}}\frac{X}{\text{nM}} \qquad (13)$$

with the prefactor $\alpha = 0.186$ for 0.1 mol% and $\alpha = 1.86$ for 1 mol% anchor lipids.

The curvature-concentration relationship in eqn (13) implies that the GFP-generated spontaneous curvature m is quite large. Indeed, it follows from eqn (13) with a mole fraction of 1 mol% anchor lipids that the spontaneous curvature m has the value $m = 1/(23\ \text{nm})$ for the protein concentration $X = 23.4$ nM and that $m = 1/(540\ \text{nm})$ even for the tiny concentration $X = 1$ nM. It is interesting to note that the magnitude of the GFP-generated spontaneous curvature m as given by eqn (13) is comparable to estimates for the spontaneous curvature generated by membrane-bound amphiphysin.[80]

4.2.1 Dilute regime of membrane-bound proteins. The curvature-concentration relationship in eqn (13) also implies that the average separation of the membrane-bound GFP molecules is larger than 25 nm for the whole concentration

range studied in ref. 19. This separation is large compared to the lateral size of a single GFP molecule, which is about 3 nm.[81] Therefore, the curvature-concentration relationship in eqn (13) corresponds to a dilute regime, in which the membrane-bound GFPs are well-separated from each other and mutual contacts between these molecules can be ignored.

4.3 Stability regime of two-sphere vesicles

The first step towards the division of giant vesicles is to prepare two-sphere or (1 + 1)-sphere vesicles with closed membrane necks that are stable with respect to neck opening. The corresponding stability regime covers a large subregion of the morphology diagram as determined theoretically and observed experimentally, see Fig. 8 and 9.

4.3.1 Theoretical stability regime for positive two-spheres. The preparation of a positive (1 + 1)-sphere vesicle can be guided by the theoretically predicted stability regime for positive (1 + 1)-spheres as displayed in Fig. 8. Inspection of this figure reveals that such vesicle shapes are stable against neck opening for spontaneous curvatures $\bar{m} > \sqrt{2}$ and for volume-to-area ratios $\bar{v}$ that are located between two lines of limit shapes denoted by L_{1+1}^{pos} and L_{2*}^{pos}. The limit shapes L_{1+1}^{pos} consist of one large and one small sphere with the effective mean curvature $M_{\mathrm{ls}}^{\mathrm{eff}} = m$ of the membrane neck corresponding to the equality in eqn (2). The limit shapes L_{2*}^{pos} consist of two equally sized spheres, which are located at $\bar{v} = 1/\sqrt{2}$ and $\bar{m} \geq \sqrt{2}$.

The geometry of (1 + 1)-spheres depends only on the volume-to-area ratio $\bar{v}$ but is independent of the spontaneous curvature $\bar{m}$.[30,50] Therefore, when we move in the stability regime of Fig. 8 along a horizontal line with constant $\bar{v}$ but increasing $\bar{m}$, the shape of the vesicle remains unchanged. Likewise, the geometry of $(N_{\mathrm{l}} + N_{\mathrm{s}})$-spheres depends only on $\bar{v}$, N_{l} and N_{s} but not on $\bar{m}$,[30,50] which implies that the multispherical shape does not change when we increase the spontaneous curvature $\bar{m}$ for constant volume-to-area ratio $\bar{v}$ and fixed sphere numbers N_{l} and N_{s}.

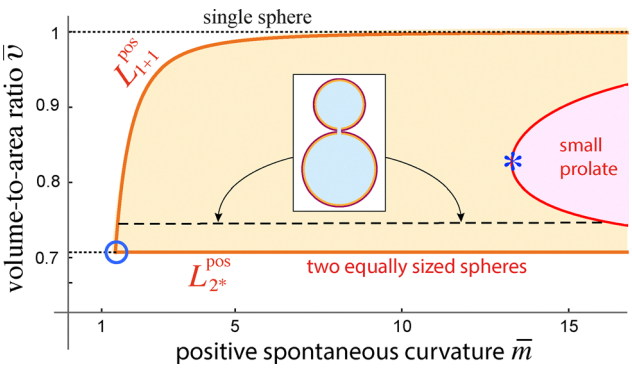

Fig. 8 Stability regime (orange) for positive two-spheres with positive spontaneous curvature $\bar{m}$. This stability regime is bounded by two lines (dark orange) of limit shapes, L_{1+1}^{pos} and L_{2*}^{pos}, which meet at the corner point (blue open circle) with $\bar{m} = \sqrt{2}$ and $v = 1/\sqrt{2}$. Along the red line enclosing the pink subregime, the small sphere transforms into a small prolate; the blue star is located at $\bar{m}_{\mathrm{ss}}$ = 13.29 and v_{ss} = 0.8259. The inset displays a persistent (1 + 1)-shape, which varies with $\bar{v}$ but does not depend on $\bar{m}$ and, thus, remains unchanged along the horizontal dashed line with a constant $\bar{v}$-value.

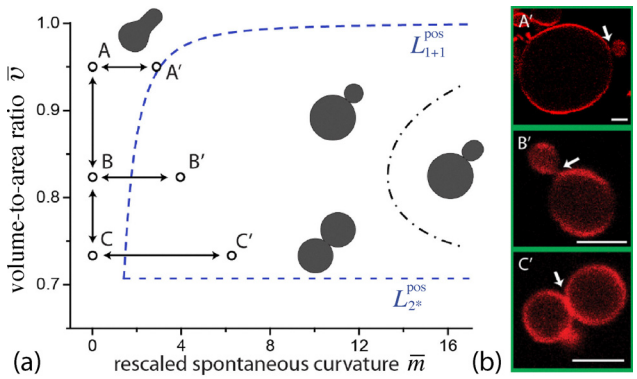

Fig. 9 (a) Morphology diagram for two-sphere vesicles as determined experimentally; and (b) corresponding two-sphere shapes A′, B′, and C′ as observed by confocal microscopy. The closed membrane necks in (b) are indicated by white arrows. All scale bars: 5 μm.[19]

4.3.2 Experimental stability regime for positive two-spheres. The experimentally observed stability regime for (1 + 1)-spheres is depicted in Fig. 9a. This stability regime is enclosed by the same two lines of limit shapes, L_{1+1}^{pos} and L_{2*}^{pos}, as in Fig. 8. Three examples for (1 + 1)-spheres are denoted by A′, B′, and C′. The corresponding optical images are shown in Fig. 9b with white arrows pointing towards the closed membrane necks of the GUVs.

4.4 Neck fission by constriction forces

Each positive membrane neck as displayed in Fig. 9b is subject to a constriction force f^{pos} as given by[19,30]

$$f^{\mathrm{pos}} = 8\pi\kappa\,(m - M_{\mathrm{ls}}^{\mathrm{eff}}) \qquad (14)$$

with the bending rigidity κ and the effective curvature $M_{\mathrm{ls}}^{\mathrm{eff}}$ of the (ls)-neck as in eqn (1). This expression for the constriction force can be derived from the bending energy E_{be} of the outbudded vesicle in the limit of vanishing neck radius R_{ne}. This bending energy has the asymptotic behavior[30]

$$E_{\mathrm{be}}(R_{\mathrm{ne}}) \approx E_{\mathrm{be}}(R_{\mathrm{ne}} = 0) + f^{\mathrm{pos}} R_{\mathrm{ne}} \quad \text{for small } R_{\mathrm{ne}}. \qquad (15)$$

Note that the constriction force f^{pos} in eqn (14) is positive for $m > M_{\mathrm{ls}}^{\mathrm{eff}}$, which corresponds to the inequality in eqn (2). This inequality defines the stability regime for (1 + 1)-spheres as depicted by the orange subregion in Fig. 8. Furthermore, the constriction force f^{pos} in eqn (14) vanishes for $m = M_{\mathrm{ls}}^{\mathrm{eff}}$, corresponding to the limit shapes L_{1+1}^{pos} as described by the equality in eqn (2). It is also meaningful to consider negative constriction forces, $f^{\mathrm{pos}} < 0$, which act to increase the neck radius and thus represent dilation forces. For the (1 + 1)-spheres displayed in Fig. 9b, the constriction force varies over the range 5.5 pN $\lesssim f^{\mathrm{pos}} \lesssim$ 142 pN when we vary the GFP concentration in the exterior solution.[19] The same force range has been estimated for the constriction forces *in vivo* as generated by the proteins dynamin,[37] ESCRT-III[82] and FtsZ.[43]

4.4.1 Vesicle division *via* neck fission. As the nanomolar concentration X of His-tagged GFP is increased in the exterior solution, the spontaneous curvature m, which is proportional to X according to eqn (13), also increases. Likewise, as m becomes larger, so does the constriction force $f^{\rm pos}$ as given by eqn (14). A larger constriction force implies a smaller free energy barrier for neck fission as well as an increased fission rate as explained in the following paragraphs. Therefore, by increasing the GFP concentration in the exterior solution, we lower the free energy barrier until the membrane neck undergoes fission, which leads to the division of the giant vesicle into two daughter vesicles as in Fig. 10.

4.5 Free energy landscape and barrier for neck fission

After the GUV has attained a dumbbell shape with closed membrane necks, as indicated by the white arrows in Fig. 9b, the fission of these necks transforms the one-vesicle (1-V) dumbbell states into two-vesicle (2-V) states consisting of two separate daughter vesicles as shown in Fig. 10. The corresponding free energy landscape is schematically displayed in Fig. 11a where the 1-V and 2-V states are separated by a free energy barrier (BA). On nanoscopic scales, one may envisage this barrier to arise from a cut across the membrane neck as depicted in Fig. 11b. This cut creates two bilayer pores, which are bounded by two ring-like bilayer edges, at which the hydrophobic core of the vesicle bilayer is in partial contact with the aqueous solutions. When these two pores close *via* the hydrophobic effect, we obtain two separate daughter vesicles as in Fig. 10 and 11a.

4.5.1 Estimate for free energy barrier. The free energy barrier separates the 1-V state before division from the 2-V state after division. A simple estimate for the height of this barrier can be obtained as follows. A cut through the neck as in Fig. 11b creates two bilayer pores. The radius of these pores is comparable to the outer radius $R_{\rm ne}$ of the closed membrane neck, which is equal to the bilayer thickness $\ell_{\rm me} \backsimeq 4$ nm. The resulting free energy barrier is governed by the bilayer edges of these two pores, at which the hydrophobic core of the vesicle bilayer is partially exposed to the surrounding aqueous solutions. The associated edge free energy is equal to the edge tension $\lambda_{\rm ed}$ times the combined circumference $4\pi\ell_{\rm me}$ of the two pores, which leads to the estimate $\Delta G_{\rm BA} \backsimeq 4\pi\ell_{\rm me}\lambda_{\rm ed}$ for the height of the free energy barrier.

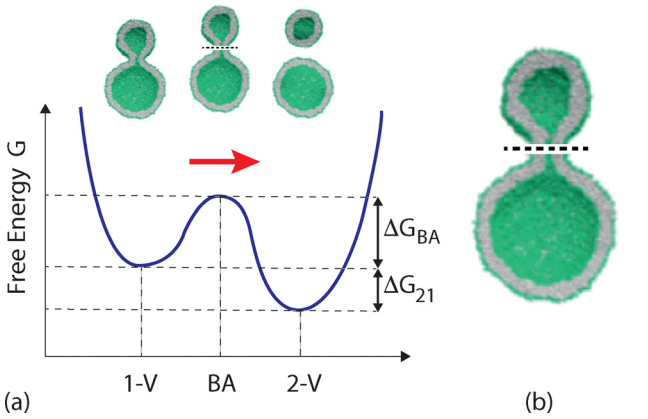

Fig. 11 (a) Schematic free energy landscape for the division of a nanovesicle.[51] For this process to be exergonic or 'downhill', the free energy difference $\Delta G_{21} \equiv G_2 - G_1$ between the 2-vesicle state (2-V) and the 1-vesicle state (1-V) must be negative. In such a situation, the fission process can proceed spontaneously without being coupled to an active process such as nucleotide hydrolysis. The rate, at which this process proceeds, is determined by the barrier height $\Delta G_{\rm BA}$, that is, by the free energy difference between the intermediate barrier (BA) state and the 1-V state; and (b) enlarged view of the intermediate BA state for the fission process, which determines the barrier height $\Delta G_{\rm BA}$ by forming two bilayer pores above and below the horizontal dashed line, which indicates a cut through the closed neck. The two pores are bounded by two bilayer edges, at which the hydrophobic core of the vesicle bilayer is in partial contact with the aqueous solutions.

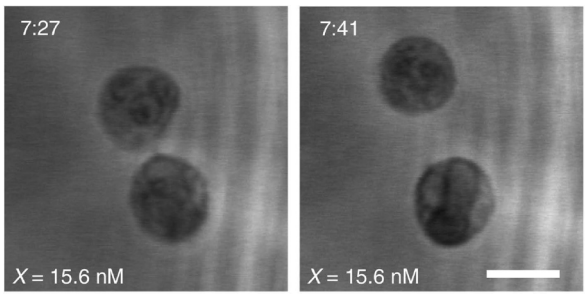

Fig. 10 Controlled division of a giant vesicle: initially, the vesicle forms a two-sphere shape with a closed neck when it is exposed to a 0.78 nM concentration of His-tagged GFP in the exterior solution. After about 2 min, the exterior GFP concentration X is increased to X = 15.6 nM, which then leads, after about 7 min, to the fission of the membrane neck and to the division of the vesicle. Therefore, the membrane-bound GFP generates a large positive spontaneous curvature as in eqn (13) which leads to a sufficiently large constriction force $f^{\rm pos}$ as given by eqn (14), to cleave the neck. Scale bar: 5 μm.[19]

To overcome this barrier, the constriction force $f^{\rm pos}$ acting against the closed neck must expend mechanical work of the order of $f^{\rm pos}\ell_{\rm me}$, thereby decreasing the neck radius $R_{\rm ne}$ from $R_{\rm ne} \backsimeq \ell_{\rm me}$ to $R_{\rm ne} = 0$. Using the expression for the constriction force $f^{\rm pos}$ in eqn (14), we then conclude that the membrane neck is likely to undergo fission if[30]

$$f^{\rm pos}\ell_{\rm me} = 8\pi\kappa(m - M_{\rm ne}^{\rm eff})\ell_{\rm me} \gtrsim \Delta G_{\rm BA} = 4\pi\ell_{\rm me}\lambda_{\rm ed} \quad (16)$$

or, equivalently, if the excess curvature $m - M_{\rm ne}^{\rm eff}$ exceeds the threshold value $\lambda_{\rm ed}/(2\kappa)$. The edge tension $\lambda_{\rm ed}$ is expected to be reduced by the constriction force, which compresses the neck and can lead to a local thinning of the lipid bilayer close to the neck.

4.5.2 Free energy barrier from Gaussian curvature energy. The 1-V and 2-V states in Fig. 11a have essentially the same bending energy $E_{\rm be}$ as obtained from eqn (10), because the closed neck of the 1-V dumbbell state is limited to a relatively small membrane area and hardly contributes to this energy. However, the two states have different topologies which implies that the Gaussian curvature energy $E_{\rm G}$ in eqn (9) makes a different contribution to the 1-V and 2-V states.

The 1-V state before fission is topologically equivalent to a single sphere with topological genus $\mathfrak{g} = 0$ and Euler

characteristic $\chi = 2$ whereas the 2-V state after fission is characterized by $\chi = 4$ and $\mathfrak{g} = -1$. It then follows that the topological transformation from the 1-V to the 2-V state changes the Gaussian curvature energy E_G by

$$\Delta E_G \equiv E_G\,(2\text{-V}) - E_G\,(1\text{-V}) = 4\pi\kappa_G, \qquad (17)$$

which represents the main contribution of the vesicle's curvature energy to the free energy difference ΔG_{21} in Fig. 11a. Because the GUVs in Fig. 9b and 10 undergo fission in the absence of any active process or chemomechanical coupling, the fission processes from the 1-V to the 2-V states must be exergonic or 'downhill' in free energy as in Fig. 11a, which implies that the free energy difference ΔG_{21} must be negative as in Fig. 11a. Using the estimate $\Delta G_{21} \backsimeq \Delta E_G$ with the change ΔE_G of the Gaussian curvature energy as given by eqn (17), we then conclude that the Gaussian curvature modulus κ_G must be negative.[19,30]

Previous experimental studies[83,84] and computer simulations[85] provide evidence that the Gaussian curvature modulus can indeed be negative with $\kappa_G \backsimeq -\kappa$. For the GUV membranes in Fig. 9, the bending rigidity κ was measured to be $\kappa \backsimeq 48k_BT$,[19] which implies the estimate $\kappa_G \backsimeq -\kappa \backsimeq -48k_BT$ and leads to the free energy difference $\Delta G_{21} \backsimeq \Delta E_G = 4\pi\kappa_G \backsimeq -603k_BT$. Therefore, the division of the GUVs in Fig. 9 and 10 is a strongly exergonic process and can occur spontaneously in the absence of any active process.

5 Active closure and opening of membrane necks

The controlled division of GUVs as described in the previous section proceeds without the chemomechanical coupling to any active process. Intuitively, one would expect that such a coupling facilitates the division process. In the present section, we look at GUVs that contain Min proteins in their interior solutions. The binding of the Min proteins to the inner leaflets of the vesicle bilayers is coupled to ATP hydrolysis.[86,87] This coupling generates active shape oscillations of the GUV which involve the recurrent closure and opening of the membrane neck as displayed in Fig. 12.[18,20] However, somewhat surprisingly, this coupling to ATP hydrolysis does not lead to the fission of the membrane neck. As explained further below, this absence of neck fission and vesicle division is intimately related to the stability regime of (1 + 1)-vesicles as depicted in Fig. 8.

5.1 Binding of Min proteins to GUV membrane

The interior solution of the GUV in Fig. 12 contains two Min proteins, MinD and MinE, as well as ATP. The Min proteins bind to and unbind from the inner leaflet of the GUV membrane. When loaded with ATP, MinD forms dimers (or oligomers)[88–91] that attach to the inner leaflet. Subsequently, MinE binds to membrane-bound MinD, and the resulting MinD–ATP–MinE complex stimulates ATP hydrolysis by MinD, causing both proteins to unbind again from the membrane. These molecular processes at the molecular scale are amplified

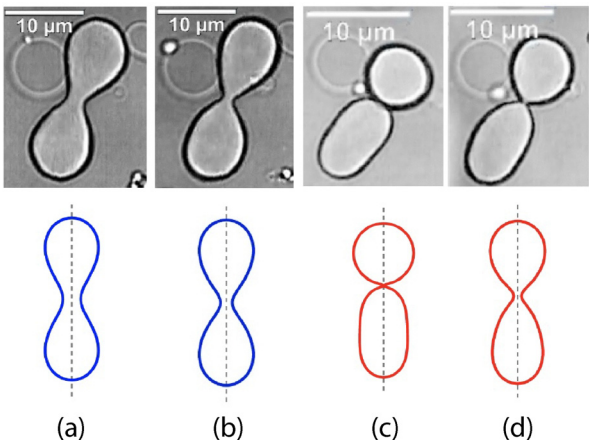

Fig. 12 Active shape oscillations of a giant vesicle that forms a dumbbell-shape with cyclic closure and opening of its membrane neck: comparison of experimentally observed[18] with theoretically calculated vesicle shapes.[20] All vesicle shapes are axi-symmetric; the axes of rotational symmetry are provided by the vertical dashed lines in the bottom row with the theoretical shapes. Each shape oscillation involves both up-down symmetric vesicle shapes (blue) and shapes (red) for which this symmetry is broken. The four shapes in (a)–(d) represent a complete cycle with an average cycle time of 55.9 s. After (d), the up-down symmetry is restored and the vesicle shape goes back to (a). The neck radius R_{ne} is equal to 1.17 μm in (a), 0.78 μm in (b), 0.12 μm in (c) and 0.52 μm in (d). The cyclic process is driven by Min proteins and ATP hydrolysis.

to the micron scale by the GUV membrane, which undergoes active shape oscillations coupled to ATP hydrolysis as displayed in Fig. 12.

Inspection of Fig. 12 shows that the experimentally observed vesicle shapes in the top row are well described by the theoretically calculated shapes in the bottom row. These calculations are based on a time-dependent spontaneous curvature m and on the minimization of the bending energy for each instantaneous m-value.[20] This approach is justified by the separation of time scales between the time period of the Min oscillations, which is about one minute,[92,93] and the time it takes a giant vesicle to relax to a new stable state, which is only a few seconds.[94,95]

As a result of such a minimization procedure, the spontaneous curvature is found to have positive values for all vesicle shapes in Fig. 12. This sign of the spontaneous is curvature is unexpected because the Min proteins bind to the inner leaflet of the GUV, in contrast to the His-tagged GFP molecules that bind to the outer leaflets of the GUVs in Fig. 9b. However, the positive values of the spontaneous curvatures generated by the Min proteins are consistent with the view that the MinD proteins dimerize in the presence of ATP and then bind to membranes *via* the C-terminal sequences of the two MinD monomers.[88–91] Such a membrane-bound MinD dimer resembles a polymer chain that is anchored to the membrane at both ends. If the average separation of the two anchor points exceeds a small fraction of the polymer's end-to-end distance, the membrane bends away from the anchored polymer,[96,97] which leads to a positive sign of the spontaneous curvature for the GUV membrane in Fig. 12.

5.2 Cyclic closure and opening of membrane neck

The active shape oscillations of the GUV involve the cyclic closure and opening of the membrane neck. In fact, the GUV in Fig. 12 undergoes 26 complete shape oscillations, corresponding to a total time period of about 24 minutes. Fig. 12 displays one oscillation cycle, which involves both vesicle shapes (blue) with an up-down symmetry as well as shapes (red), for which this symmetry is broken. The cycle in Fig. 10 is completed by the symmetry-restoring transformation from panel (d) to panel (a) and has an average time period of 55.9 s.[20]

The cyclic closure and opening of the membrane neck as shown in Fig. 12 implies that the constriction force also oscillates between positive and negative values. Indeed, neck closure from panel (a) to panel (b) and from panel (b) to panel (c) requires a positive constriction force, $f^{\rm pos} > 0$, whereas neck opening from panel (c) to panel (d) and from panel (d) to panel (a) requires a negative constriction force, $f^{\rm pos} < 0$. This conclusion is confirmed by computing the constriction force $f^{\rm pos}$ *via* eqn (14), using the *m*-values as obtained by the best fit of the theoretical and experimental shapes, see Fig. 12.§

5.3 Theoretical analysis of experimental observations

The theoretically computed shapes in the lower row of Fig. 12 are obtained from the shape equation for axi-symmetric shapes.[20,47] The volume-to-area ratio $\bar{v}$ as given by eqn (12) has the constant value $\bar{v} = 0.670$ during the whole shape oscillation. Comparison with the stability regime in Fig. 8 reveals that this value of $\bar{v}$ is somewhat below the line of limit shapes $L_{2*}^{\rm pos}$ which is located at $\bar{v} = 1/\sqrt{2} = 0.707$. Therefore, the different shapes of the GUV as displayed in Fig. 12 are located somewhat below the stability regime for (1 + 1)-spheres. This conclusion is in agreement with the numerical values of the oscillating neck radius. Indeed, the largest neck radius is found to be 1.17 μm as in Fig. 12a whereas the smallest neck radius is 0.12 μm or 120 nm as in Fig. 12c. Even though the latter neck radius is not resolvable by conventional optical microscopy, this radius is still much larger than the radius of a closed neck, which is about 4 nm, corresponding to the thickness of the lipid bilayer.

5.4 Prevention of neck fission

As previously explained in Section 4.4, the free energy barrier for neck fission can be estimated from the two bilayer edges that are created by cutting the neck as in Fig. 11b. For a closed neck with radius $R_{\rm ne} \backsimeq \ell_{\rm me}$, the two bilayer edges create the free energy barrier of height $\Delta G_{\rm BA} \backsimeq 4\pi\ell_{\rm me}\lambda_{\rm ed}$ with the edge tension $\lambda_{\rm ed}$. For an open neck with radius $R_{\rm ne} \gg \ell_{\rm me}$, this free energy barrier is increased to $\Delta G_{\rm BA} \backsimeq 4\pi R_{\rm ne}\lambda_{\rm ed}$. Furthermore, the smallest neck radius for the oscillating vesicle in Fig. 12 is given by $\min(R_{\rm ne}) = 120$ nm, corresponding to Fig. 12c. Therefore, the fission of this neck has to overcome a free energy barrier that is increased by at least a factor $\min(R_{\rm ne})/\ell_{\rm me} \backsimeq 30$ compared to the barrier for a closed neck. We thus conclude that all dumbbell shapes in Fig. 12 involve very large free energy barriers for the fission of their membrane necks, which prevents this fission and, thus, the division of the GUV.

§ In this computation, the effective mean curvature $M_{\rm ls}^{\rm eff}$ of the experimentally observed shapes is approximated by the corresponding curvature of the limit shapes L_{2*} which have the same *m*-values as the experimental shapes.

6 Giant vesicles with intramembrane domains

6.1 Intramembrane domains in multi-component membranes

Biological and biomimetic membranes are fluid, contain several molecular ocmponents, and represent two-dimensional systems. From a theoretical point of view, such membranes should be able to undergo phase separation into two distinct fluid domains, in close analogy to liquid mixtures in two or three dimensions.[98,99] This theoretical prediction about fluid–fluid coexistence in membranes has now been firmly established by many experimental studies, in particular for GUV membranes consisting of ternary lipid mixtures.[13,21,100–104] In fact, fluid–fluid coexistence has even been found in giant plasma membrane vesicles that contain a wide assortment of different lipids and proteins.[105,106]

6.2 Domain-induced budding

Intramembrane domains are enclosed by a domain boundary with a line free energy that is proportional to the length of this boundary. The line free energy per unit length defines the line tension $\lambda_{\rm db}$ of the domain boundary, which is always positive and acts to shorten the domain boundary. The competition between the line tension $\lambda_{\rm db}$ and the vesicles's bending energy leads to the budding of intramembrane domains as predicted theoretically[98,99,107,108] and confirmed by several experimental studies of GUVs.[13,14,21,102,103,109,110]

6.3 Neck closure and multispheres

Vesicles with two intramembrane domains, denoted by a and b, can form two-sphere vesicles when their volume is reduced by osmotic deflation as depicted in Fig. 13. For a b-domain with a

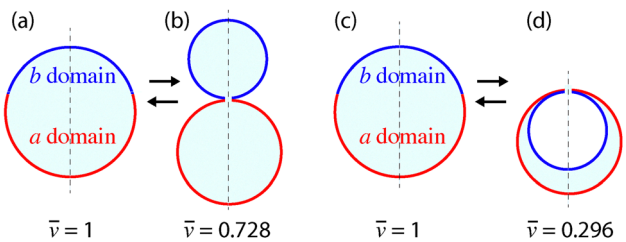

Fig. 13 Shape transformations of spherical vesicles consisting of one a-domain (red) with positive spontaneous curvature and one b-domain (blue) with positive or negative spontaneous curvature $m_{\rm b}$: (a,b) for positive $m_{\rm b}$, the spherical vesicle in (a) transforms into an out-budded two-sphere vesicle as in (b); and (c,d) for negative $m_{\rm b}$, the spherical vesicle in (c) transforms into an in-budded two-sphere vesicle as in (d). In both cases, the volume-to-area ratio $\bar{v}$ is reduced by osmotic deflation (→) from $\bar{v} = 1$ for the initial spherical shapes to $\bar{v} < 1$ for the final two-sphere shapes. This transformation is reversible so that the initial shape can be recovered by osmotic inflation (←).[111]

positive bilayer asymmetry and, thus, a positive spontaneous curvature $m_b > 0$, the volume reduction leads to an out-budded (1 + 1)-sphere as in Fig. 13b. On the other hand, for a b-domain with a negative bilayer asymmetry and, thus, a negative spontaneous curvature $m_b < 0$, the volume reduction leads to an in-budded (1 + 1)-sphere as in Fig. 13d. More precisely, the stability conditions for the closed necks in Fig. 13 involve both the mean curvatures of the two spheres as well as the two spontaneous curvatures m_a and m_b of the a and b domains. In addition, these stability conditions can involve the line tension λ_{db} of the (ab)-domain boundary depending on the Gaussian curvature moduli of the two domains.[111]

6.4 Intramembrane domains with distinct bilayer asymmetries

Using microfluidics, GUV membranes have been recently prepared that possess different lipid compositions in their two leaflets and, in addition, form intramembrane domains a and b with distinct bilayer asymmetries.[27] Additional contributions to these asymmetries arise from anchor lipids that prefer one of the two membrane domains and bind different proteins from the exterior and/or interior solutions. As a consequence, one can now fine-tune the spontaneous curvatures m_a and m_b of the a and b domains independently. The GUVs prepared in this way form membrane necks that undergo fission as displayed in Fig. 14.

6.5 Curvature discontinuity along domain boundary

The theory of curvature elasticity leads to the prediction that the mean curvature of a GUV membrane is discontinuous across the ab domain boundary and attains two different values, $M_{a,db}$ and $M_{b,db}$ on the a- and b-side of this boundary. The discontinuity of the mean curvature is described by the matching condition[111]

$$\kappa_a\left[m_a - M_{a,db}\right] - \kappa_b\left[m_b - M_{b,db}\right] = \frac{1}{2}(\kappa_{Ga} - \kappa_{Gb})C_{\|db} \quad (18)$$

where the a and b domains have the spontaneous curvatures m_a and m_b, the bending rigiditie κ_a and κ_b as well as the two Gaussian curvature moduli κ_{Ga} and κ_{Gb}, and $C_{\|db}$ represents the second principal curvature parallel to the domain boundary, which is continuous across this boundary. For the limiting case, in which both domains have the same curvature-elastic parameters, the matching condition in eqn (18) reduces to $m = \frac{1}{2}\left[M_{a,db} + M_{b,db}\right]$, which is identical to the neck closure condition for limit shapes as given by $m = M_{ls}^{eff}$ in eqn (2) and (3). The curvature discontinuity as given by eqn (18) has been confirmed by a systematic analysis of the observed out-budded vesicle shape, see the first image in Fig. 14.[27]

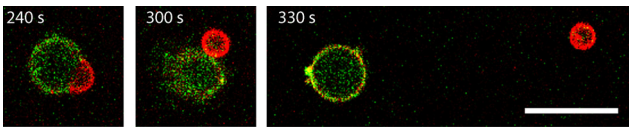

Fig. 14 Time series of confocal images for the division of a GUV with two intramembrane domains, a liquid-ordered (red) and a liquid-disordered (green) domain.[27] In the first image at time t = 240 s, the red domain forms a bud with an open domain boundary and an open membrane neck. In the second image at t = 300 s, this open neck has become closed and the red domain forms a spherical out-bud. The last image at t = 330 s demonstrates that the closed neck undergoes fission, thereby dividing the two-domain GUV into a green and a red daughter vesicle. Scale bar: 20 μm. A detailed analysis of the first image reveals that the membrane exhibits a discontinuity along the domain boundary as predicted theoretically.[111]

7 GUV division by ESCRT proteins

ESCRT proteins are involved in many cellular processes and in particular in the fission of membrane necks *via* the formation of ESCRT filaments that bind to membrane segments close to the membrane neck. The ESCRT-induced fission of membrane necks can be demonstrated by *in vitro* experiments for the division of GUVs based on a minimal set of three ESCRT-III proteins from yeast cells (*Saccharomyces cerevisiae*)[4] and from parasitic protozoa (*Entamoeba histolytica*).[5,9] In the present context, it is important to emphasize that this minimal set of three ESCRT-III proteins achieves GUV fission without any coupling to an active process. *In vivo*, the ESCRT complex also involves ATP hydrolysis by a membrane ATPase such as Vps3 but this coupling to ATP hydrolysis is only required for the disassembly of the ESCRT complex from the membrane after the neck fission has been completed.[4]

7.1 Sequential remodeling of GUVs by three ESCRT-III proteins

The remodeling of GUVs by three ESCRT-III proteins can be dissected into three sequential remodeling steps corresponding to protein binding to the GUV membranes, formation of membrane necks, and division of GUVs by fission of membrane necks.[4,5,9] First, when added to the exterior solution, the ESCRT-III protein¶ EhVps20 is bound to the GUV membrane; this membrane forms in-buds after the addition of the second ESCRT-III protein EhVps32, which is an ortholog of the protein Snf7 in yeast; finally, the membrane necks of the in-buds undergo fission and the in-buds are released as small intraluminal vesicles into the interior of the giant vesicle when the third ESCRT-III protein EhVps24 is added to the exterior solution. None of the three ESCRT-III proteins EhVps20, EhVps32, and EhVps24 hydrolyses ATP. The sequential remodeling of GUVs by the three ESCRT-III proteins is displayed in Fig. 15.

7.2 Models for the neck closure by ESCRT-III proteins

Several models have been proposed to explain how the membrane-bound ESCRT proteins lead to closed membrane necks and generate a sufficiently large constriction force at the membrane neck to cleave this neck.[112] In these models, the proteins are assumed to form a layer that adheres to the membrane segment close to the neck. Two such models are displayed in Fig. 16. In the dome model,[113,114] the protein layer

¶ The prefix "Eh" stands for *Entamoeba histolytica*.

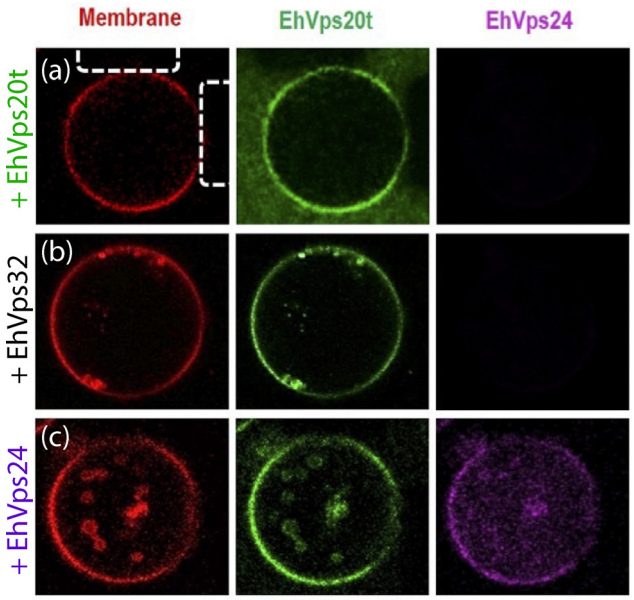

Fig. 15 Sequential remodeling of an individual GUV membrane (red) by three ESCRT-III proteins, which are added to the exterior solution: (a) binding of EhVps20 (green) to the GUV membrane; (b) binding of EhVps32 (unlabeled) leads to the formation of many in-buds connected to the mother vesicle by membrane necks; and (c) binding of EhVps24 (purple) leads to fission of the in-buds which are then released as intraluminal vesicles (red) into the interior solution.[5,9]

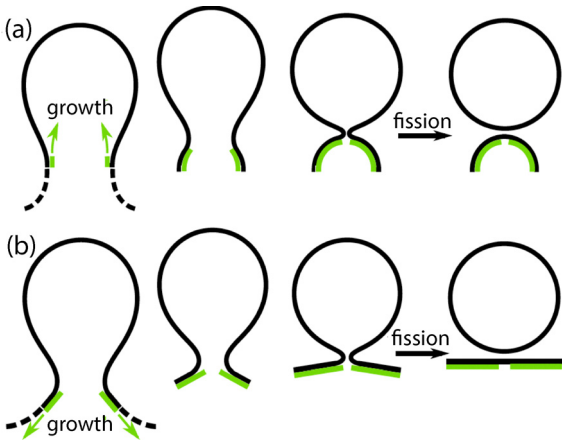

Fig. 16 Two theoretical models for the fission of a membrane neck by ESCRT-III proteins, which bind to the inner leaflet of the neck and assemble into a protein layer at the membrane: (a) in the dome model,[113,114] the protein layer grows towards the in-bud (green arrows), thereby forming a dome-like scaffold for the membrane neck; and (b) in the spiral spring or cone-flattening model,[114,115] the protein layer grows away from the in-bud (green arrows), forming a cone-like scaffold for the neck that may flatten during the growth process. In both (a) and (b), the membrane-bound protein layer generates a constriction force onto the membrane neck, which depends on the adhesion free energy between protein layer and membrane.[114]

grows into a dome-like scaffold as schematically shown in Fig. 16a. In the spiral spring or cone flattening model,[114,115] on the other hand, the protein layer forms a cone-like scaffold as in Fig. 16b that flattens during its growth. For both models, one can compute the constriction force generated by the protein layers at the membrane neck.[114] This force is predicted to vary from 60 to 100 pN in the dome model and from 100 to 140 pN in the flattening cone model.

8 Giant vesicles in contact with condensate droplets

Condensate droplets are formed by liquid–liquid phase separation in aqueous solutions of macromolecules such as polymers and proteins. Such macromolecular solutions, also known as aqueous two-phase systems, have been applied for a long time in biochemical analysis and biotechnology[116] and are intimately related to water-in-water emulsions.[117,118] The interactions of condensate droplets with vesicles leads to a variety of different morphologies of the vesicle-droplet systems such as partial and complete wetting of the membranes by the droplets; in-budding and out-budding of the vesicle membranes; complete engulfment of the droplets by the vesicle membrane; formation of membrane nanotubes, which can attain multi-spherical, cylindrical, or unduloidal shapes; transformations from nanotubes to nanosheets consisting of membrane "pancakes".[32] Here, we will focus on the complete engulfment of the condensate droplets by the vesicle membranes because these engulfment processes create closed membrane necks as displayed in Fig. 17.

8.1 Complete engulfment of condensate droplets

Aqueous phase separation leads to the formation of two coexisting liquid phases, denoted by α and β. In general, both the exterior aqueous solution outside of the vesicle and the interior aqueous solution within the vesicle can undergo phase separation. The condensate droplets are then formed by nucleation of the minority phase which occupies a smaller volume fraction after phase separation compared to the majority phase. In general, the minority phase is determined by the overall concentrations of the macromolecular solution. In Fig. 17a and b, the minority phase is provided by the β phase which is formed by nucleation within the majority phase α; in Fig. 17c and d, the β droplet occupies a volume fraction that is larger than the volume fraction of the α droplet.

Complete engulfment of condensate droplets as shown in Fig. 17 is driven by a relatively large interfacial tension of the $\alpha\beta$-interface between the two coexisting liquid phases α and β. More precisely, the vesicle-droplet system leads to complete engulfment if the interfacial tension $\Sigma_{\alpha\beta}$ is large compared to the curvature-elastic tensions $\sigma_{\alpha\gamma} = 2\kappa_{\alpha\gamma}m_{\alpha\gamma}^2$ and $\sigma_{\beta\gamma} = 2\kappa_{\beta\gamma}m_{\beta\gamma}^2$ of the $\alpha\gamma$ and $\beta\gamma$ membrane segments in contact with the α and β phases.[32]

8.2 Different pathways for the closure of membrane necks

The closed membrane necks displayed in Fig. 17 are formed by the closure of open membrane necks. The neck closure process can proceed *via* different morphological pathways which are distinguished by the sign of the constriction force f acting at the

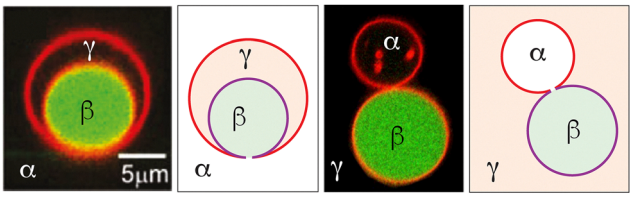

Fig. 17 Complete engulfment of condensate droplets: (a) and (b) confocal microscopy image and schematic drawing of a completely engulfed β droplet, formed by nucleation within the majority phase α in the exterior aqueous solution.[119] The contact line neck is characterized by a negative value of the effective mean curvatue; and (c) and (d) image and drawing of completely engulfed α and β droplets arising from phase separation in the interior aqueous solution.[120] In all panels, the third liquid phase γ is a spectator phase, which is not involved in the phase separation.

neck. The constriction force f depends on the curvarure-elastic parameters of the two membrane segments $\alpha\gamma$ and $\beta\gamma$ and may also depend on the line tension λ_{cl} of the contact line between the membrane and the droplet. More precisely, the constriction force f depends on the line tension λ_{cl} if the contact line radius R_{cl} vanishes together with the neck radius R_{ne} as the neck closes.[32,111]

However, the contact line radius may attain a finite limit when the neck radius vanishes. One example for such a behavior is depicted in Fig. 18, which applies to Gaussian curvature moduli $\kappa_{G,\beta\gamma}$ and $\kappa_{G,\alpha\gamma}$ that satisfy $\kappa_{G,\alpha\gamma} < \kappa_{G,\beta\gamma}$. In such a situation, the closed membrane neck is formed by the $\beta\gamma$ membrane segment and the associated constriction force f is then given by

$$f = 8\pi\kappa_{\beta\gamma}(m_{\beta\gamma} - M_{ij}^{\mathrm{eff}}) \qquad (19)$$

for positive spontaneous curvature, $m_{\beta\gamma} > 0$, with the effective mean curvature M_{ij}^{eff} of the closed neck. As before, M_{ij}^{eff} is a purely geometric geometry that is positive for necks connecting two spherical membrane segments i and j with positive mean curvatures M_i and M_j. On the other hand, if the Gaussian curvature moduli of the two membrane segments satisfy the inequality $\kappa_{G,\alpha\gamma} > \kappa_{G,\beta\gamma}$, the membrane neck is formed by the $\alpha\gamma$ segment and the corrresponding constriction force is obtained from eqn (19) by replacing all subscripts $\beta\gamma$ in this equation by subscripts $\alpha\gamma$.

8.2.1 Neck closure for positive constriction forces. For a positive constriction force, $f > 0$, and different Gaussian curvature moduli, $\kappa_{G,\alpha\gamma} \neq \kappa_{G,\beta\gamma}$, of the two membrane segments, the contact line is shifted away from the closing membrane neck as schematically shown in Fig. 18 for $\kappa_{G,\alpha\gamma} < \kappa_{G,\beta\gamma}$. Estimating the Gaussian curvature moduli in terms of the bending rigidities *via* $\kappa_{G,\alpha\gamma} \backsimeq -\kappa_{\alpha\gamma}$ and $\kappa_{G,bg} \backsimeq -\kappa_{\beta\gamma}$, the inequality $\kappa_{G,\alpha\gamma} < \kappa_{G,\beta\gamma}$ implies the inequality $\kappa_{\alpha\gamma} > \kappa_{\beta\gamma}$. The closing neck is then formed by the $\beta\gamma$ membrane segment with the less negative Gaussian curvature modulus and the smaller bending rigidity. Furthermore, the shift of the contact line away from the neck's waistline as in Fig. 18 also has the consequence that the contact line attains a finite radius R_{cl} in the limit of zero neck radius $R_{ne} = 0$.

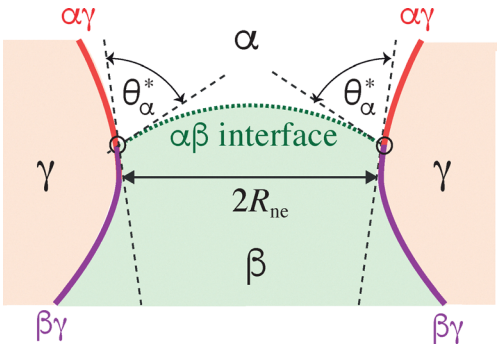

Fig. 18 Axisymmetric membrane neck (purple/red) spanned by a small segment of the $\alpha\beta$ interface (dotted green), which has the shape of a spherical cap and forms the intrinsic contact angle θ_α^* with the $\alpha\gamma$ membrane segment (red). The radius R_{cl} of the circular contact line exceeds the radius R_{ne} of the circular waistline of the neck. Such a displacement of the contact line away from the neck's waistline represents one possible pathway for the axisymmetric neck closure when the two membrane segments have different Gaussian curvature moduli $\kappa_{G,\alpha\gamma}$ and $\kappa_{G,\beta\gamma}$ with $\kappa_{G,\alpha\gamma} < \kappa_{G,\beta\gamma}$.[32]

8.2.2 Neck closure for negative constriction forces. For a negative constriction force, $f < 0$, the vesicle-droplet system is governed by a combination of the membrane's bending energy and the interfacial free energy of the $\alpha\beta$ interface, which is proportional to the interfacial tension $\Sigma_{\alpha\beta}$. In the limit of small neck radius R_{ne}, the free energy E_{2Dr} of the two-sphere shape in Fig. 17c and d has the asymptotic behavior[32]

$$E_{2Dr}(R_{ne}) = E_{2Dr}(R_{ne} = 0) - |f|R_{ne} + c_{\alpha\beta}\Sigma_{\alpha\beta}R_{ne}^2 \qquad (20)$$

with the dimensionless coefficient $c_{\alpha\beta} \equiv 2\pi/(1 + \sin\theta_\alpha^*) > 0$. The free energy in eqn (20) exhibits a local mimimum at

$$R_{ne} = |f|/(2c_{\alpha\beta}\Sigma_{\alpha\beta}), \qquad (21)$$

corresponding to a narrow neck with finite radius $R_{ne} > 0$.

8.2.3 Absence of neck fission and vesicle division. As shown in Fig. 19b, complete engulfment by giant vesicle membranes has been observed for phase separation of interior PEG-dextran solutions, generating two spherical subcompartments, with one subcompartment enclosing the PEG-rich α droplet whereas the other subcompartment was filled with the dextran-rich β droplet. However, these two subcompartments remained connected by a long membrane nanotube as in Fig. 19c, which implies that the membrane neck did not undergo fission.[120] The elongation of the membrane neck into a membrane nanotube has also been observed in ref. 121 where the nanotubes were denoted as "tethers". This morphological pathway is unique to contact line necks of membranes in contact with condensate droplets and is not possible for domain boundary necks of two-domain vesicles as discussed in Section 6. Indeed, the latter vesicles do not involve an $\alpha\beta$ interface and their energy does not include the interfacial free energy $E_{\alpha\beta} \sim \Sigma_{\alpha\beta}R_{ne}^2$, which is, however, necessary in order to stabilize a narrow neck with finite radius $R_{ne} > 0$ as described by eqn (21) and displayed in Fig. 19c.

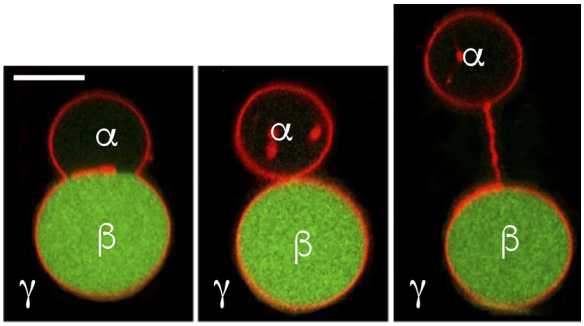

Fig. 19 (a) Giant vesicle membrane (red) enclosing a PEG-rich droplet α (black) and a dextran-rich droplet β (green). The vesicle is surrounded by the spectator phase γ (black); (b) osmotic deflation of the vesicle leads to the formation of a membrane neck that connects the spherical membrane segments around the α and β droplets; and (c) further deflation of the vesicle leads to the elongation of the membrane neck into a membrane nanotube between the two spherical membrane segments. Scale bar: 25 μm. Reused with permission from ref. 120, John Wiley and Sons, 2017.

9 Nanovesicles in contact with condensate droplets

In the previous section about giant vesicles in contact with condensate droplets, we discussed several pathways for the closure of the membrane neck. On the one hand, the membrane necks were taken to close in an axisymmetric manner, which represents the usual assumption in the literature. On the other hand, the membrane necks of the giant vesicles adjacent to the condensate droplets did not undergo fission.

In contrast, complete engulfment followed by neck fission has been observed in molecular dynamics simulations, which also revealed that the closed membrane neck can attain an unusual tight-lipped shape that prevents the fission of this neck.[31,122] Whether the vesicle-droplet system takes the axisymmetric or the non-axisymmetric pathway for the closure of the membrane neck depends on the line tension λ_{cl} of the contact line. In contrast to the line tension λ_{db} of a domain boundary, the line tension of a contact line can be positive or negative. In fact, the sign of the contact line tension is controlled by the stress asymmetry $\Delta\Sigma_{ve} = \Sigma_{ol} - \Sigma_{il}$ between the two leaflet tensions Σ_{il} and Σ_{ol} as shown by extensive molecular dynamics simulations.[31] These simulations revealed that the line tension is negative for relatively small stress asymmetries, including the case of symmetric bilayers, but becomes positive for relatively large stress asymmetries.

9.1 Fission of axisymmetric membrane necks

For relatively large stress asymmetries between the two bilayer leaflets, the contact line tension is positive and the membrane neck adjacent to the condensate droplet closes in an axisymmetric manner as shown in Fig. 20. Such a closure process leads to the fission of the membrane neck and the division of the nanovesicle, see last snapshot in Fig. 20 at time t = 12 μs.

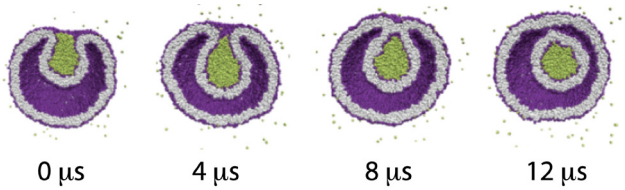

Fig. 20 Endocytosis of condensate droplet (green) *via* axisymmetric engulfment, followed by the division of the nanovesicle (purple-grey) into two nested daughter vesicles: at time t = 0 μs, the droplet is partially engulfed by the vesicle membrane, which forms an open membrane neck. At t = 4 μs, the neck closes and the droplet becomes completely engulfed. The neck undergoes fission at t = 9 μs, generating a small intraluminal vesicle around the droplet. The vesicle membrane contains N_{ol} = 5500 lipids in its outer and N_{il} = 4600 lipids in its inner leaflet. Such an axisymmetric process is observed for positive line tensions, $\lambda_{cl} > 0$, of the contact line.[31]

If the droplet size is too large, complete engulfment is not possible without membrane rupture.[30,31] This geometric constraint is obvious from an intuitive point of view and follows from the isoperimetric inequality.[31,123–125] In such a situation, the engulfment process is terminated when the droplet has been engulfed only partially, that is, when the contact area between droplet and membrane is significantly smaller than the surface area of the droplet.

9.2 Tight-lipped shape of membrane neck

The complete engulfment of the droplet can also proceed in a non-axisymmetric manner and then leads to a strongly non-circular contact line and to a tight-lipped shape of the closed membrane neck.[31] Such an unusual neck shape, which prevents the fission of this neck, see the time-lapse snapshots in Fig. 21, was first observed in molecular dynamics simulations for complete engulfment of condensate droplets by planar bilayers.[122] Tight-lipped membrane necks are also formed during the endocytosis of rigid nanoparticles.[29]

10 Summary and outlook

This paper addresses the division of vesicles *via* the formation and fission of closed membrane necks as studied by theory, experiment, and simulations. Using the effective mean curvature M_{ij}^{eff} of closed necks as in eqn (4), we can distinguish positive from negative necks, a distinction that can be generalized to positive and negative multispheres as illustrated in Fig. 4. For GUV membranes with a laterally uniform composition, both positive and negative necks are governed by simple stability relations as given by eqn (2) and (3). These stability relations provide inequalities between the effective mean curvature M_{ij}^{eff} of the membrane neck and the spontaneous curvature m. The effective mean curvature is a purely geometric quantity that can be directly deduced from the optical images of GUVs.

The stability regime for positive two-sphere vesicles is displayed in Fig. 8. This stability regime has been confirmed experimentally by studying GUVs doped with His-tagged GFP

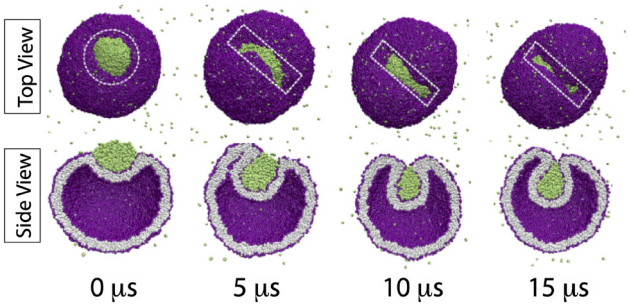

Fig. 21 Non-axisymmetric engulfment of condensate droplet (green), leading to a tight-lipped shape of the membrane neck that prevents neck fission: vesicle bilayer (purple-grey) with N_{ol} = 5963 lipids in its outer and N_{il} = 4137 lipids in its inner leaflet. At t = 0, the droplet is partially engulfed by the vesicle membrane with an axisymmetric contact line, as indicated by the white dashed circle. The axial symmetry is broken at t = 5 μs, as follows from the strongly non-circular and highly elongated contact lines for $t \geq 5$ μs, as indicated by the white dashed rectangles. Such a non-axisymmetric process is observed for negative line tensions, $\lambda_{cl} < 0$, of the contact line.[31]

(Fig. 9). The GFP molecules bind from the exterior solution to anchor lipids within the GUV membranes as in Fig. 7. The coverage of the membrane by the protein molecules can be controlled by the mole fraction of the anchor lipids and by the nanomolar protein concentration in the exterior solution. As a result, one finds that the spontaneous curvature m increases linearly with the nanomolar protein concentration X as described by eqn (13). In addition, the theory predicts that the constriction force f^{pos} at a positive neck is proportional to the excess curvature $(m - M_{ij}^{eff})$ as in eqn (14). For a sufficiently large constriction force, the closed membrane neck undergoes fission as observed experimentally for a sufficiently large increase of the GFP concentration in the exterior solution (Fig. 10). The free energy landscape for neck fission and vesicle division is provided in Fig. 11 with a visualization of the corresponding free energy barrier.

Membrane necks can undergo active shape oscillations between open and nearly closed states as described in Section 5 and displayed in Fig. 12. These oscillations are driven by Min proteins that bind to the inner leaflet of the GUV membrane and hydrolyze ATP. The GUV displayed in Fig. 10 undergoes 26 complete oscillations with an average oscillation period of 55.9 s. Thus, the nearly closed membrane neck is stable against fission for at least 24 minutes. The smallest neck radius is estimated to be 120 nm (Fig. 12c), which cannot be resolved by conventional light microscopy but is still sufficiently large to create a high energy barrier that prevents the fission of the neck. The absence of neck fission for the GUV in Fig. 12 provides strong evidence that the vesicles need to form (almost) closed membrane necks in order to undergo division *via* neck fission.

Closed membrane necks can also be formed by the osmotic deflation of GUVs with intramembrane domains as schematically shown in Fig. 13. The division of such vesicles with positive membrane necks has been recently observed experimentally, see the example in Fig. 14. Likewise, the formation and fission of negative necks can be induced by three ESCRT-III proteins and then leads to intraluminal vesicles as displayed in Fig. 15.

On the other hand, GUVs in contact with condensate droplets form two-sphere shapes as illustrated in Fig. 17 but the membrane necks of these shapes did not undergo fission so far. Instead, the necks were observed to become extended into long nanotubes as displayed in Fig. 19. The absence of neck fission for these vesicle-droplet systems can be explained by the competition between the interfacial tension $\Sigma_{\alpha\beta}$ of the droplets with a negative constriction force, $f < 0$, as described by eqn (20) and (21).

Droplet-induced fission has, however, been observed in molecular dynamics simulations for positive line tension of the contact line as shown in Fig. 20. These simulations also revealed that a negative contact line tension leads to closed membrane necks with an unusual, tight-lipped shape as in Fig. 21.

The view presented here can be further scrutinized by future studies. One interesting topic is to vary the geometric and/or curvature-elastic parameters for the shape oscillations of vesicles with Min proteins (Fig. 12) because it should be possible to truncate these oscillations and to induce neck fission by binding additional molecules to the outer leaflet of the GUV. Another interesting topic is to vary the curvature-elastic parameters of the GUVs exposed to condensate droplets, thereby finding parameter values that lead to vesicle division. Using molecular dynamics simulations, one should be able to study the behavior of domain boundaries and contact lines during neck closure of nanovesicles. These studies will further eludicate the concept of Gaussian curvature moduli at the nanoscale.

Finally, the behavior of membrane necks as discussed here for biomimetic membranes will also be relevant for cellular membranes. One example is the remodeling of intracellular membranes by enveloped viruses which create replication factories connected to these membranes. Two examples for such a virus-induced remodeling of the membrane architecture are displayed in Fig. 22 for the membrane of the endoplasmic reticulum.

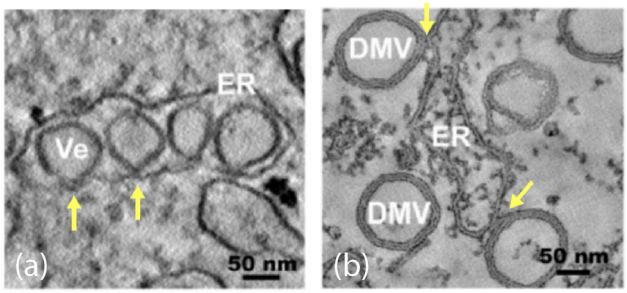

Fig. 22 Remodeling of the endoplasmic reticulum (ER) by viruses that create replication factories: electron tomographs of replication factories as built by dengue viruses in (a) and by hepatitis C viruses in (b). The ER membrane in (a) forms in-budded vesicles (Ve) with inward-pointing membrane necks, whereas the ER membrane in (b) is reshaped into out-budded double-membrane vesicles (DMV) with outward-pointing membrane necks. Some of the necks are indicated by yellow arrows. Scale bars: 50 nm.[126]

Conflicts of interest

There are no conflicts to declare.

Data availability

This paper analyzes and elucidates the results of recent experimental studies and computer simulations about the division of giant unilamellar vesicles (GUVs) and nanovesicles. All experimental and simulation data are published and available in the list of references of this manuscript.

Acknowledgements

This article is based on a talk that I gave at the Technical University in memory of Erich Sackmann, who was a very inspiring scientist and had a strong influence on the biophysics community in Germany. I first met Erich after he had initiated the Sonderforschungsbereich (Center of Excellence) 266 about ''Synthetic and Biological Interfaces'' and had invited me to become a principal investigator of this consortium. I then had the pleasure to visit his lab at the TU Munich several times. His lab involved a huge crowd of students, resembling a very lively bee-hive. Erich strongly interacted with his students, always willing to get involved into some scientific discussions. I also had many inspiring discussions with him about a wide range of membrane topics. Sometimes, our discussions had rather strong side effects. In the early 1990ies, for example, Erich and I travelled to a conference in Vancouver and had a stopover at the airport in Frankfurt. We started to discuss about membranes in general and about lipid protrusions in particular. Our discussion became quite intense and rather long. As a consequence, we were late at the departure gate, missed our plane to Vancouver, and lost our luggage! In the first half of the 1990ies, we had many meetings as editors of the handbook on ''Structure and dynamics of membranes'' that was published in 1995. Thus, I am grateful to Erich Sackmann for many stimulating discussions and important insights into the behavior of membranes and vesicles. I also thank all of my colleagues who have participated in the research described here for fruitful and enjoyable collaborations. This work was supported by the Max Planck Institute of Colloids and Interfaces as well as by the Max Planck Society and the Dieter Schwarz foundation *via* the Max Planck School ''Matter to Life''. Open Access funding provided by the Max Planck Society.

Notes and references

1 K. Berndl, J. Käs, R. Lipowsky, E. Sackmann and U. Seifert, *Europhys. Lett.*, 1990, **13**, 659–664.
2 A.-L. Bernarda, M.-A. Guedeau-Boudevillea, L. Jullien and J.-M. di Meglio, *Biochim. Biophys. Acta*, 2002, **1567**, 1–5.
3 A. Ambrožič, T. B. Božič, T. Kveder, J. Majhenc, V. Arrigler, S. Svetina and B. Rozman, *Biochim. Biophys. Acta*, 2005, **1740**, 38–44.
4 T. Wollert, C. Wunder, J. Lippincott-Schwartz and J. H. Hurley, *Nature*, 2009, **458**, 172–177.
5 Y. Avalos-Padilla, R. L. Knorr, R. Javier-Reyna, G. Garca-Rivera, R. Lipowsky, R. Dimova and E. Orozco, *Front. Cell. Infect. Microbiol.*, 2018, **8**, 53.
6 T. Bhatia, S. Christ, J. Steinkühler, R. Dimova and R. Lipowsky, *Soft Matter*, 2020, **16**, 1246–1258.
7 S. Penič, L. Mesarec, M. Fošnarič, L. Mrówczyńska, H. Hägerstrand, V. Kralj-Iglič and A. Iglič, *Front. Phys.*, 2020, **8**, 342.
8 X. Liu, J. Stenhammar, H. Wennerström and E. Sparr, *J. Phys. Chem. Lett.*, 2022, **13**, 498–507.
9 Y. Avalos-Padilla, V. Gregoriev, E. Ewins, T. Robinson, E. Orozco, R. Lipowsky and R. Dimova, *iScience*, 2023, **26**, 105765.
10 P. D. Sambre, J. C. S. Ho and A. N. Parikh, *J. Am. Chem. Soc.*, 2024, **146**, 3250–3261.
11 R. Kumar, R. Chakrabarti and R. M. Thaokar, *Soft Matter*, 2024, **20**, 6995–7011.
12 H.-G. Döbereiner, J. Käs, D. Noppl, I. Sprenger and E. Sackmann, *Biophys. J.*, 1993, **65**, 1396–1403.
13 T. Baumgart, S. Hess and W. Webb, *Nature*, 2003, **425**, 821–824.
14 K. A. Riske, N. Bezlyepkina, R. Lipowsky and R. Dimova, *Biophys. Rev. Lett.*, 2006, **1**, 387–400.
15 J. Sanborn, K. Oglecka, R. S. Kraut and A. N. Parikh, *Faraday Discuss.*, 2013, **161**, 167–176.
16 C. Pernpeintner, J. A. Frank, P. Urban, C. R. Roeske, S. D. Pritzl, D. Trauner and T. Lohmüller, *Langmuir*, 2017, **33**, 4083–4089.
17 V. N. Georgiev, A. Grafmüller, D. Bléger, S. Hecht, S. Kunstmann, S. Barbirz, R. Lipowsky and R. Dimova, *Adv. Sci.*, 2018, **5**, 1800432.
18 T. Litschel, B. Ramm, R. Maas, M. Heymann and P. Schwille, *Angew. Chem., Int. Ed.*, 2018, **57**, 16286–16290.
19 J. Steinkühler, R. L. Knorr, Z. Zhao, T. Bhatia, S. Bartelt, S. Wegner, R. Dimova and R. Lipowsky, *Nat. Commun.*, 2020, **11**, 905.
20 S. Christ, T. Litschel, P. Schwille and R. Lipowsky, *Soft Matter*, 2021, **17**, 319–330.
21 Y. Dreher, K. Jahnke, E. Bobkova, J. P. Spatz and K. Göpfrich, *Angew. Chem., Int. Ed.*, 2021, **60**, 10661–10669.
22 Y. Dreher, K. Jahnke, M. Schröter and K. Göpfrich, *Nano Lett.*, 2021, **21**, 5952–5957.
23 N. Y. Kostina, A. M. Wagner, T. Haraszti, K. Rahimi, Q. Xiao, M. L. Klein, V. Percec and C. Rodriguez-Emmenegger, *Soft Matter*, 2021, **17**, 254–267.
24 Y. Miele, G. Holló, I. Lagzi and F. Rossi, *Life*, 2022, **12**, 841.
25 P. Zambrano, X. Chen, C. M. E. Kriebisch, B. A. K. Kriebisch, O. Zozulia and J. Boekhoven, *J. Am. Chem. Soc.*, 2024, **146**, 33359–33367.
26 I. Schachter, *Biophys. J.*, 2025, **124**, 1741–1746.
27 N. Yandrapalli, T. Seemann, R. Lipowsky and T. Robinson, *Nat. Commun.*, 2026, **17**, 2620.
28 R. Ghosh, V. Satarifard, A. Grafmüller and R. Lipowsky, *Nano Lett.*, 2019, **19**, 7703–7711.

29 R. Lipowsky, R. Ghosh, V. Satarifard, A. Sreekumari, M. Zamaletdinov, B. Różycki, M. Miettinen and A. Grafmüller, *Biomolecules*, 2023, **13**, 926.
30 R. Lipowsky, *The Giant Vesicle Book*, Taylor & Francis, 2019, ch. 5, pp. 73–168.
31 R. Ghosh, V. Satarifard and R. Lipowsky, *Nat. Commun.*, 2023, **14**, 615.
32 R. Lipowsky, *Soft Matter*, 2025, **21**, 7370–7392.
33 A. Lehninger, D. Nelson and M. Cox, *Principles of biochemistry*, Worth Publishers, New York, 2nd edn, 1993.
34 T. Hill, *Free Energy Transduction in Biology*, Academic Press, New York, 1st edn, 1977.
35 K. Takel, P. S. McPherson, S. L. Schmidt and P. D. Camilli, *Nature*, 1995, **374**, 186–190.
36 S. M. Sweitzer and J. E. Hinshaw, *Cell*, 1998, **93**, 1021–1029.
37 A. Roux, G. Koster, M. Lenz, B. Sorre, J.-B. Manneville, P. Nassoy and P. Bassereau, *Proc. Natl. Acad. Sci. U. S. A.*, 2010, **107**, 4141–4146.
38 M. Babst, B. Wendland, E. J. Estepa and S. D. Emr, *EMBO J.*, 1998, **17**, 2982–2993.
39 M. A. Y. Adell, S. M. Migliano and D. Teis, *FEBS J.*, 2016, **283**, 3288–3302.
40 P. de Boer, R. Crossley and L. Rothfield, *Nature*, 1992, **359**, 254–256.
41 D. RayChaudhuri and J. T. Park, *Nature*, 1992, **359**, 251–254.
42 H. P. Erickson, D. E. Anderson and M. Osawa, *Microbiol. Mol. Biol. Rev.*, 2010, **74**, 504–528.
43 J. Xiao and E. D. Goley, *Curr. Opin. Microbiol.*, 2016, **34**, 90–96.
44 M. Osawa and H. P. Erickson, *Proc. Natl. Acad. Sci. U. S. A.*, 2013, **110**, 11000–11004.
45 D. A. Ramirez-Diaz, D. A. Garcia-Soriano, A. Raso, J. Mücksch, M. Feingold, G. Rivas and P. Schwille, *PLoS Biol.*, 2018, **16**, e2004845.
46 D. A. Ramirez-Diaz, A. Merino-Salomón, F. Meyer, M. Heymann, G. Rivas, M. Bramkamp and P. Schwille, *Nat. Commun.*, 2021, **12**, 3310.
47 U. Seifert, K. Berndl and R. Lipowsky, *Phys. Rev. A:At., Mol., Opt. Phys.*, 1991, **44**, 1182–1202.
48 B. Fourcade, L. Miao, M. Rao, M. Wortis and R. Zia, *Phys. Rev. E:Stat. Phys., Plasmas, Fluids, Relat. Interdiscip. Top.*, 1994, **49**, 5276–5286.
49 R. Lipowsky, *Adv. Colloid Interface Sci.*, 2014, **208**, 14–24.
50 R. Lipowsky, *Adv. Colloid Interface Sci.*, 2022, **301**, 102613.
51 R. Lipowsky, *Adv. Biol.*, 2022, **6**, 2101020.
52 M. Zamaletdinov, M. Miettinen and R. Lipowsky, *Soft Matter*, 2023, **19**, 6929–6944.
53 A. Sreekumari and R. Lipowsky, *Soft Matter*, 2022, **18**, 6066–6078.
54 L. D. Landau and E. M. Lifshitz, *Theory of Elasticity*, Pergamon Press, New York, 1986.
55 W. Helfrich, *Z. Naturforsch.*, 1973, **28c**, 693–703.
56 M. do Carmo, *Differential geometry of curves and surfaces*, Prentice-Hall, Englewood Cliffs, NJ, USA, 1976.
57 R. Lipowsky, *Faraday Discuss.*, 2013, **161**, 305–331.
58 T. Bhatia, J. Agudo-Canalejo, R. Dimova and R. Lipowsky, *ACS Nano*, 2018, **12**, 4478–4485.
59 H. Deuling and W. Helfrich, *J. Phys.*, 1976, **37**, 1335–1345.
60 J. Litster, *Phys. Lett.*, 1975, **53A**, 193–194.
61 C. Taupin, M. Dvolaitzky and C. Sauterey, *Biochemistry*, 1975, **14**, 4771–4775.
62 M. M. Kozlov, *Soft Condensed Matter Physics in Molecular and Cell Biology*, CRC Press, Hoboken, 2006, pp. 79–95.
63 F. Campelo, C. Arnarez, S. J. Marrink and M. M. Kozlov, *Adv. Colloid Interface Sci.*, 2014, **208**, 25–33.
64 M. M. Kozlov and L. V. Chernomordik, *Curr. Opin. Struct. Biol.*, 2015, **33**, 61–67.
65 B. Pontesa, P. Monzo and N. C. Gauthier, *Semin. Cell Dev. Biol.*, 2017, **71**, 30–41.
66 E. Alipour, D. Halverson, S. McWhirter and G. C. Walker, *Annu. Rev. Phys. Chem.*, 2017, **68**, 261–283.
67 P. V. Bashkirov, P. I. Kuzmin, J. V. Lillo and V. A. Frolov, *Annu. Rev. Biophys.*, 2022, **51**, 473–497.
68 B. Derjaguin, N. Churaev and V. Muller, *Surfaces forces*, Consultants Bureau, New York, 1987.
69 C. Isenberg, *The Science of Soap Films and Soap Bubbles*, Dover Publications, New York, 1992.
70 C. Radke, *J. Colloid Interface Sci.*, 2015, **449**, 462–479.
71 R. Lipowsky, *Faraday Discuss.*, 2025, **259**, 234–263.
72 W. Helfrich and W. Harbich, *Chem. Scr.*, 1985, **25**, 32–36.
73 L. Peliti and S. Leibler, *Phys. Rev. Lett.*, 1985, **54**, 1690–1693.
74 G. Gompper and D. Kroll, *Phys. Rev. E:Stat. Phys., Plasmas, Fluids, Relat. Interdiscip. Top.*, 1995, **51**, 514–525.
75 T. V. Tolpekina, W. K. den Otter and W. J. Briels, *J. Chem. Phys.*, 2004, **121**, 8014–8020.
76 O. Farago, *J. Chem. Phys.*, 2003, **119**, 596–605.
77 J. W. Gibbs, *The Scientific Papers of J. Willard Gibbs*, Longman, Green, and Co., 1906, vol. I.
78 J. Rowlinson and B. Widom, *Molecular Theory of Capillarity*, Oxford University Press, Oxford, 1989.
79 S. Pramanik, J. Steinkühler, R. Dimova, J. P. Spatz and R. Lipowsky, *Soft Matter*, 2022, **18**, 6372–6383.
80 B. Sorre, A. Callan-Jones, J. Manzi, B. Goud, J. Prost, P. Bassereau and A. Roux, *Proc. Natl. Acad. Sci. U. S. A.*, 2012, **109**, 173–178.
81 J. A. J. Arpino, P. J. Rizkallah and D. D. Jones, *PLoS One*, 2012, **7**, e47132.
82 J. Schoeneberg, M. R. Pavlin, S. Yan, M. Righini, I.-H. Lee, L.-A. Carlson, A. H. Bahrami, D. H. Goldman, X. Ren, G. Hummer, C. Bustamante and J. H. Hurley, *Science*, 2018, **362**, 1423–1428.
83 A. Derzhanski, A. G. Petrov and M. D. Mitov, *Ann. Phys.*, 1978, **3**, 297.
84 S. Lorenzen, R.-M. Servuss and W. Helfrich, *Biophys. J.*, 1986, **50**, 565–572.
85 M. Hu, J. J. Briguglio and M. Deserno, *Biophys. J.*, 2012, **102**, 1403–1410.
86 Z. Hu, E. P. Gogol and J. Lutkenhaus, *Proc. Natl. Acad. Sci. U. S. A.*, 2002, **99**, 6761–6766.
87 M. Loose, E. Fischer-Friedrich, C. Herold, K. Kruse and P. Schwille, *Nat. Struct. Mol. Biol.*, 2011, **18**, 577–583.

88 J. Lutkenhaus and M. Sundaramoorthy, *Mol. Microbiol.*, 2003, **48**, 295–303.
89 Z. Hu and J. Lutkenhaus, *Mol. Microbiol.*, 2003, **47**, 345–355.
90 W. Wu, K.-T. Park, T. Holyoak and J. Lutkenhaus, *Mol. Microbiol.*, 2011, **79**, 1515–1528.
91 T. Heermann, B. Ramm, S. Glaser and P. Schwille, *J. Mol. Biol.*, 2020, **432**, 3191–3204.
92 A. Dajkovic and J. Lutkenhaus, *J. Mol. Microbiol. Biotechnol.*, 2006, **11**, 140–151.
93 K. Zieske and P. Schwille, *eLife*, 2014, **3**, e03949.
94 F. Brochard and J. Lennon, *J. Phys.*, 1975, **36**, 1035–1047.
95 H. Duwe, J. Käs and E. Sackmann, *J. Phys.*, 1990, **51**, 945–962.
96 C. Hiergeist, PhD thesis, Universität Potsdam, Potsdam, Germany, 1997.
97 R. Lipowsky, H. G. Döbereiner, C. Hiergeist and V. Indrani, *Phys. A*, 1998, **249**, 536–543.
98 R. Lipowsky, *J. Phys. II*, 1992, **2**, 1825–1840.
99 R. Lipowsky, *Biophys. J.*, 1993, **64**, 1133–1138.
100 C. Dietrich, L. Bagatolli, Z. Volovyk, N. Thompson, M. Levi, K. Jacobson and E. Gratton, *Biophys. J.*, 2001, **80**, 1417–1428.
101 S. Veatch and S. Keller, *Biophys. J.*, 2003, **85**, 3074–3083.
102 K. Bacia, P. Schwille and T. Kurzchalia, *Proc. Natl. Acad. Sci. U. S. A.*, 2005, **102**, 3272–3277.
103 N. Bezlyepkina, R. S. Graciá, P. Shchelokovskyy, R. Lipowsky and R. Dimova, *Biophys. J.*, 2013, **104**, 1456–1464.
104 S. F. Fenz and K. Sengupta, *Integr. Biol.*, 2012, **4**, 982–995.
105 T. Baumgart, A. T. Hammond, P. Sengupta, S. T. Hess, D. A. Holowka, B. A. Baird and W. W. Webb, *Proc. Natl. Acad. Sci. U. S. A.*, 2007, **104**, 3165–3170.
106 S. L. Veatch, P. Cicuta, P. Sengupta, A. Honerkamp-Smith, D. Holowka and B. Baird, *ACS Chem. Biol.*, 2008, **3**, 287–293.
107 F. Jülicher and R. Lipowsky, *Phys. Rev. Lett.*, 1993, **70**, 2964–2967.
108 F. Jülicher and R. Lipowsky, *Phys. Rev. E:Stat. Phys., Plasmas, Fluids, Relat. Interdiscip. Top.*, 1996, **53**, 2670–2683.
109 T. Baumgart, S. Das, W. W. Webb and J. T. Jenkins, *Biophys. J.*, 2005, **89**, 1067–1080.
110 S. Semrau, T. Idema, L. Holtzer, T. Schmidt and C. Storm, *Phys. Rev. Lett.*, 2008, **100**, 088101.
111 R. Lipowsky, *Eur. Phys. J. E:Soft Matter Biol. Phys.*, 2024, **47**, 4.
112 J. Schöneberg, I.-H. Lee, J. H. Iwasa and J. H. Hurley, *Nat. Rev. Mol. Cell Biol.*, 2017, **38**, 5.
113 G. Fabrikant, S. Lata, J. D. Riches, J. A. G. Briggs, W. Weissenhorn and M. M. Kozlov, *PLoS Comput. Biol.*, 2009, **5**, e1000575.
114 J. Agudo-Canalejo and R. Lipowsky, *PLoS Comput. Biol.*, 2018, **14**, e1006422.
115 N. Chiaruttini, L. Redondo-Morata, A. Colom, F. Humbert, M. Lenz, S. Scheuring and A. Roux, *Cell*, 2015, **163**, 866–879.
116 P. A. Albertsson, *Partition of Cell Particles and Macromolecules: Separation and Purification of Biomolecules, Cell Organelles Membranes, and Cells in Aqueous Polymer Two-Phase Systems and Their Use in Biochemical Analysis and Biotechnology*, Wiley, 3rd edn, 1986.
117 L. Piculell and B. Lindman, *Adv. Colloid Interface Sci.*, 1992, **41**, 149–178.
118 J. Esquena, *Curr. Opin. Colloid Interface Sci.*, 2016, **25**, 109–119.
119 Y. Li, H. Kusumaatmaja, R. Lipowsky and R. Dimova, *J. Phys. Chem. B*, 2012, **116**, 1819–1823.
120 R. Dimova and R. Lipowsky, *Adv. Mater. Interfaces*, 2017, **4**, 1600451.
121 M. Andes-Koback and C. D. Keating, *J. Am. Chem. Soc.*, 2011, **133**, 9545–9555.
122 V. Satarifard, A. Grafmüller and R. Lipowsky, *ACS Nano*, 2018, **12**, 12424–12435.
123 R. Osserman, *Bull. Am. Math. Soc.*, 1978, **84**, 1182–1238.
124 S. Hildebrandt and A. Tromba, *Mathematics and Optimal Form*, American Scientific Library, New York, NY, USA, 1985.
125 R. Lipowsky, *Membranes*, 2023, **13**, 223.
126 I. Romero-Brey and R. Bartenschlager, *Viruses*, 2014, **6**, 2826–2857.

